Contents lists available at ScienceDirect

Engineering Geology

journal homepage: www.elsevier.com/locate/enggeo

Analytical and numerical models of debris flow impact

Sabatino Cuomo [a,*], Angela Di Perna [a], Mario Martinelli [b,c]

[a] University of Salerno, Italy
[b] Deltares, Delft, Netherlands
[c] Technical University of Delft, Netherlands

ARTICLE INFO

Keywords:
Mechanism
Mitigation
Structure
Material Point Method
Numerical

ABSTRACT

A full understanding of the interaction mechanisms among flow-like landslides and impacted protection structures is still an open issue. Although several approaches, from experimental to numerical, have been used so far, a thoroughly assessment of the hydromechanical behaviour of the landslide body is achievable only through a multiphase and large deformation approach.

This paper firstly proposes a conceptual model for a specific type of protection structure, namely a Deformable Geosynthetics-Reinforced Barrier (DGRB), i.e., an embankment made of coarse-grained soil layers reinforced by geogrids. In such a case, the sliding of the barrier along its base, under the impulsive action of a flow-type landslide, is an important landslide energy dissipation mechanism, and a key issue for the design. Then, two different approaches are proposed: i) an advanced hydro-mechanical numerical model based on Material Point Method is tested in simulating the whole complex landslide-structure interaction mechanisms, ii) an analytical model is set up to deal with the landslide energy dissipation and the kinematics of both the landslide and barrier. The calibration of the proposed analytical model is pursued based on the numerical results. Finally, the analytical model is successfully validated to interpret a large dataset of landslide impact field evidence, for whose interpretation also five empirical methods available in the literature are tested.

1. Background

The impact mechanisms regulating the interaction of a flow-like landslide with different types of barriers have been investigated by different tools, which however can be grouped in empirical, numerical and analytical.

The availability of direct measurements of the impact of flow-like masses against monitored structures has been fundamental for

Abbreviations: $\mathbf{a}_L$ (m/s^2), liquid acceleration; $\mathbf{a}_S$ (m/s^2), solid acceleration; B (m), greater base of the barrier; b (m), smaller base of the barrier; $\mathbf{b}$ (kPa), body force vector; $c'(kPa)$, effective cohesion; d (m), distance between landslide and barrier; DGRB, Deformable Geosynthetics-Reinforced Barrier; $\mathbf{D}$ (kPa), tangent stiffness matrix; dp_L (kPa), excess pore pressure; $d\boldsymbol{\sigma}'(kPa)$, increment of effective stress; E (kPa), Young modulus of soil; E_k (kJ), kinetic energy of the system; $E_{k,\,1}$ (kJ), kinetic energy of the landslide; $E_{k,\,2}$ (kJ), kinetic energy of the barrier; F_1 (kN/m), contact force along the base of the flow; F_2 (kN/m), impact force along the side of the barrier; F_3 (kN/m), contact force along the smaller base of the barrier; F_4 (kN/m), contact force along the greater base of the barrier; Fr $(-)$, Froude number; $\boldsymbol{f}_d$ (kPa), drag force vector; $\boldsymbol{g}$ (m/s^2), gravity vector; k (m^2), intrinsic permeability; k_{sat} (m/s), saturated hydraulic conductivity; $\mathbf{K}_L$ (kPa), elastic bulk modulus of the liquid; h (m), flow heigth; H (m), barrier heigth; LSI, Landslide-Structure Interaction; L_1 (m), flow length; L_2 (m), length of barrier's lateral side; MPM, Material Point Method; m_1 (kg), landslide mass; m_2 (kg), barrier mass; n $(-)$, porosity; p_L (kPa), liquid pressure; t (s), time; t_0 (s), initial reference time; t_{imp} (s), time related to *LSI* beginning; t_f (s), final time of *LSI*; T_1 (s), time related to the peak impact force; T_2 (s), final time of impact phase; V_1 (m^3), volume of the mixture; $V_{f,\,sx}$ (m^3), volume retained by the barrier; V_L (m^3), liquid phase volume; V_S (m^3), solid phase volume; $\mathbf{v}_L$ (m/s), liquid velocity vector; $\mathbf{v}_S$ (m/s), solid velocity vector; $\mathbf{v}_1$ (m/s), landslide velocity; $\mathbf{v}_2$ (m/s), barrier velocity; s (m), geometry change length; x (m), horizontal Cartesian coordinate; y (m), vertical Cartesian coordinate; τ $(-)$, ratio between T_1 and T_2; β $(^\circ)$, angle between lateral side and base of the barrier; $\Delta a_{S,\,contact}$, change in solid phase acceleration induced by the contact formulation; $\Delta a_{L,\,contact}$, change in liquid phase acceleration induced by the contact formulation; $\Delta E_k(kJ)$, dissipated kinetic energy; Δt_{cr} $(-)$, critical time step; δ $(^\circ)$, contact friction angle between flow and barrier; δ_b $(^\circ)$, contact friction angle between barrier and base; $\boldsymbol{\varepsilon}$ $(-)$, strain vector; $\varepsilon_d(-)$, cumulative deviatoric strain; κ $(-)$, static impact coefficient; λ $(-)$, geometry change parameter; μ_L $(kPa \bullet s)$, liquid dynamic viscosity; υ $(-)$, Poisson's ratio; ρ_L (kg/m^3), liquid density; ρ_m (kg/m^3), density of the mixture; ρ_S (kg/m^3), solid density; σ (kPa), total stress tensor of the mixture; $\dot{\boldsymbol{\sigma}}'$ (kPa/s), stress rate tensor of the solid phase; $\boldsymbol{\sigma}_n$ (kPa), normal stress tensor; φ' $(^\circ)$, internal friction angle; ψ $(^\circ)$, dilatancy angle; Ω, spin tensor.

* Corresponding author.
E-mail address: scuomo@unisa.it (S. Cuomo).

https://doi.org/10.1016/j.enggeo.2022.106818
Received 15 October 2021; Received in revised form 19 July 2022; Accepted 2 August 2022

investigating the main impact mechanisms. On such a topic, the literature provides few full-scale flume experiments (De Natale et al., 1999; Bugnion et al., 2012) but a large variety of reduced-scale laboratory tests (Hübl et al., 2009; Armanini et al., 2011; Canelli et al., 2012; Ashwood and Hungr, 2016; Vagnon and Segalini, 2016).

These reduced-scale laboratory tests have been used to derive and validate the most common empirical formulations used to assess the peak impact pressure in the design of protection measures against landslide (Scheidl et al., 2013; Scotton and Deganutti, 1997; Arattano and Franzi, 2003; Hübl et al., 2009; Proske et al., 2011; Bugnion et al., 2012; Canelli et al., 2012; He et al., 2016; Song et al., 2021; Di Perna et al., 2022). It is true that laboratory tests are affected by scale effects that cannot be properly monitored (Iverson, 1997; Hübl et al., 2009), but this limitation is usually overcome by appropriate scale analysis. Nevertheless, the empirical formulations greatly depend on empirical coefficients which are difficult to estimate in the practical applications due to their wide ranges of variation. In these approaches: (i) the impact load is assumed to be totally transferred to the structure without any dissipation during the impact, and (ii) the size, stiffness and inertial resistance of the artificial barrier are not considered (Vagnon and Segalini, 2016). These assumptions lead to safe assessment of the peak impact force and to overestimate the barrier design. Hence, enhancements will be proposed in this paper on both these topics.

It is also remarkable that a wide set of reduced-scale laboratory experiments on dry granular flows allowed Faug (2015) to propose a so-called phase-diagram based on: (i) Froude number (Fr) and (ii) non-dimensional height (H/h), i.e., the barrier height (H) relative to the flow depth (h). The diagram comprises four mechanisms: a) Dead zone (i.e., gradual accumulation of material behind the barrier): this is the case of relatively slow flows ($Fr \approx 1$) impacting relatively small barriers ($H/h \approx 1$); b) Airborne jet (forming downstream of the barrier): this stands for rapid flow ($Fr \gg 1$) and small barriers; c) Standing jumps (propagating downstream of the barrier with steady-state conditions): for rapid flow ($Fr \gg 1$); d) Bores (a granular jump hits the barrier and propagates upstream of it): in the case of a rapid flow hitting a very tall barrier spanning the entire height of the flow ($H/h \gg 1$) with unsteady conditions. However, pore-water pressure largely contributes to regulate the landslide-structure interaction mechanisms, whose analysis require the use of sophisticated approaches.

Numerical modelling is the most used alternative approach to tackle the analysis of Landslide-Structure Interaction (LSI). The latter has been afforded through Discrete Element Method (DEM) as reported by Leonardi et al. (2016), Calvetti et al. (2017) and Shen et al. (2018) or continuum mechanics models based on Eulerian methods (Moriguchi et al., 2009), Lagrangian particle-based methods such as Smoothed-Particle Hydrodynamics (SPH) (e.g. Bui and Fukagawa, 2013), Particle Finite Element Method (PFEM) (e.g. Idelsohn et al., 2004), Finite Element Method with Lagrangian integration points (FEMLIP) (e.g., Cuomo et al., 2013), Material Point Method (MPM), (Ceccato et al., 2018) or coupled Eulerian-Lagrangian methods (Qiu et al., 2011; Jeong and Lee, 2019). Several other numerical methods exist since years (Rabczuk and Belytschko, 2004, 2007, among others) and meshfree methods are becoming very popular. However, the solid-fluid hydro-mechanical coupling and the role of the interstitial fluid in the landslide-structure interaction have been considered only in recent times. For instance, the impact behaviour of saturated flows against rigid barriers was simulated through MPM analyses of centrifuge test results (Cuomo et al., 2021a).

Recent analytical models also investigate the LSI for various cases. Yong et al. (2019) proposed an analytical solution for estimating the sliding of a barrier under the impact of a boulder. In this case, the colliding bodies are both assumed as rigid, and the impact is studied through the elastic collision principles. However, such method cannot be applied for instance to the case of a flow-like landslide impacting a Deformable Geosynthetics-Reinforced Barrier (DGRB), i.e., an embankment made of coarse-grained soil layers reinforced by geogrids (Cuomo et al., 2020b). Li et al. (2021) proposed an analytical model to estimate the peak impact pressure that a debris flow exerts on a rigid barrier. Such model has the strength of being validated by data encompassing a wide range of distinct flow regimes, relative to real-scale observations of debris flows, small-scale experiments and recent coupled CFD-DEM simulations. Finally, Song et al. (2021) obtained an analytical model for evaluating the deflection of a flexible barrier (a net fixed to the ground) through the validation against experimental results of centrifuge tests. However, these models cannot be applied neither to estimate the impact pressure on a DGRB nor to determine the maximum displacement reached by the barrier. Hence, there is still a gap in the scientific literature and this paper will provide a contribution to such topic.

The present work analyses the impact mechanisms of flow-like landslides against greened artificial barriers such as DGRB in a large set of full-scale realistic scenarios. A Conceptual Model of Landslide-Structure Interaction (LSI) is proposed and a numerical MPM model is used to explore the main features of the hydro-mechanical interaction of saturated flows with different types of barriers. Then, a novel analytical method is casted able to reproduce the temporal evolution of both the impact forces and the kinetic energy of the flow (and also of the barrier, if the latter is free to move along its base). The analytical method is calibrated based on the numerical results, and it is later validated to satisfactorily interpret a large dataset of field evidence. The analytical method is then compared to the MPM model and to five empirical methods available in the literature. The advantages and the limitations of this new analytical method are finally discussed.

2. Exploring the landslide-structure interaction

2.1. Conceptual model

We assume that a flow-like landslide mass impacts against a DGRB, unfixed to the base ground, and free to slide over it (Fig. 2), as proposed by Cuomo et al. (2020b). The landslide body has the following features: unitary width, length L_1, depth h, density of the mixture ρ_m, initial uniform velocity $v_{1,\,0}$, pore-water pressure p_L and friction angle along the base ground equal to $\tan\varphi_b$. The geometric characteristics of the barrier are: greater base B,smaller base b, height H, inclination of the impacted side β.

The LSI problem is described through the following timelines: initial configuration (t_0), landslide propagation ($t_0 < t < t_{imp}$), impact of the landslide front (t_{imp}), time of the peak impact force (T_1), start of the inertial stage (T_2), end of LSI (t_f).

Before the landslide reaches the barrier ($t_0 < t < t_{imp}$), i.e., during the propagation stage, the LSI problem is governed by the basal frictional force F_1 (Eq. (1)), which acts along the bottom of the flow (L_1) and controls the reduction in flow velocity, resulting into a decrease of the impact forces.

When the flow interacts with the barrier ($t_{imp} < t < T_2$), additional stresses (mostly orthogonal to the impacted surface, hence horizontal in many applications) are produced at the impacted side of the barrier. Many studies (e.g., Cui et al., 2015; Song et al., 2017) demonstrated that the total impact force-time history can be simplified as a triangular force impulse, usually with a rise time (T_1) much shorter than the decay time ($T_2 - T_1$).

For the action-reaction principle, the mutual impact forces (F_2) between the landslide and the barrier are equal and opposite. Such mutual stress makes: (i) the flow to decelerate and (ii) the barrier to slip along its base and to deform itself, as shown in Fig. 2. The evaluation of the impact forces applied on the inclined side of the barrier (L_2) is fundamental to design the size and the structural characteristics of the barrier (Eq. (2)).

It is also worth noting that the flow may overtop the barrier during the impact, generating an additional force F_3 on the structure (Eq. (3)), mainly dependent on the flow-barrier frictional contact ($\tan\delta$).

After the impulsive stage of the LSI ($T_2 < t < t_f$), then the problem is mostly governed by the inertial resistance force F_4 (Eq. (4)), which depends on the amount of friction mobilized along the base (B) of the barrier ($\tan\delta_b$). The final displacement Δx of the barrier depends on both the amount of energy transferred to the barrier and that dissipated by friction.

$$F_1(t) = \int_0^{L_1(t)} (\rho_m - \rho_L) g h(x,t) tan\varphi_b dx \tag{1}$$

$$F_2(t) = \int_0^{L_2} (\rho_m - \rho_L) a(t) h(x,t) \Big/ cos\beta dx + \int_0^{L_2} p_L(x,t) \Big/ cos\beta dx \tag{2}$$

$$F_3(t) = \int_0^{b} (\rho_m - \rho_L) g h(x,t) tan\delta dx \tag{3}$$

$$F_4(t) = \frac{1}{2}\rho_b g H(b+B) tan\delta_b + \int_0^{L_2} (\rho_m - \rho_L) a(t) h(x,t) cos\beta tan\delta_b dx + \int_0^{b} (\rho_m - \rho_L) g h(x,t) tan\delta_b dx \tag{4}$$

2.2. MPM modelling

To schematize the problem in a realistic way, multiple materials are considered such as: the flow-like landslide, the barrier, and the base soil (Di Perna, 2022). The latter is necessary to ensure the frictional contact at the base of the moving barrier (Fig. 3). In such an approach the build-up of excess pore pressure in the flow material during the impact is considered as well as the hydro-mechanical coupled behaviour and the yield criterion of the flow material itself.

It is quite difficult to propose a standard landslide configuration as initial condition for modelling since it must represent the shape of the flow in a certain moment of its propagation stage. As known, this configuration strongly depends on the flow-path topography and on the geomorphological conditions that can vary from site to site. However, many studies have demonstrated that the front is often steeper and higher than the rear portion due to friction with the ground topography (Iverson, 1997; Thouret et al., 2020). For this reason, the chosen initial configuration of the landslide is characterized by a 45°-inclined front and a tail of length equal to three times the flow height. To consider different flow volumes, an i number of squares have been placed between the head and tail portions. Given this shape, the landslide has the same volume of an equivalent box with the same height h and a length $L_m = (2 + i) \bullet h$, and unitary width.

The landslide is assumed as approaching the barrier with a fixed geometric configuration and constant velocity, until LSI starts. In fact, this manuscript solely deals with LSI. It means that the landslide triggering analysis and the propagation analysis have been conducted before. The outcomes of such previous analyses are precisely the shape of the landslide (here simplified at our best as a trapezoidal shape), the thickness of the core part of the landslide, and the velocity (even assumed the same within the whole landslide body). These three factors once inserted in the numerical analyses are used as "initial values" from which their spatio-temporal evolution is computed. Such computation is not possible with the literature empirical methods, which only use the thickness and velocity to assess the peak impact action on the barrier.

For real flows, the body will be compressed by gravity during propagation and thus, a constant velocity cannot be sustained. Indeed, the presence of very differently compressed zones inside the landslide body is very important inside the triggering landslide area and during the propagation along steep slopes. At the locations where the barriers could be realistically installed, i.e., in the gentle piedmont areas, these differences in the compression of the landslide body should be less evident. However, we cannot currently assess the relevance of this simplification, which could be investigated in the future developments.

For the barrier it is assumed: dry material, frictional contact at base and rigid behaviour. This last hypothesis relates to the construction mode typically used for such kind of DGRBs, which involve the use of 0.6–0.7 m thick layers of coarse materials reinforced through geosynthetics (usually geogrids) with high tensile strength and wrapped around the facing of the barrier. In fact, recent studies outlined that any local deformation of a DGRB or a relative horizontal shifting of its layers may occur under the impact of a flow (Cuomo et al., 2020b), although the horizontal displacement along its base is the prevailing limit state of the barrier. This finding combined to the fact that both the core soil and the geogrids are very resistant materials makes the structure experiencing stress levels much lower than the ultimate values in most parts of the structure.

The Material Point Method (MPM) is used here. It is an enhancement of the Finite Element Method (FEM), and it is very well suited for large deformation problems. The continuum body consists of several Lagrangian points, named Material Points (MPs), which carry all the physical properties of the continuum such as stress, strain, density, momentum, material parameters and other state parameters. The MPs move across a background mesh, which covers the domain where the material is expected to move, and it is used to solve the governing equations without storing any permanent information.

The so-called *one-phase single-point* formulation can be opportunely adopted for dry materials. Conversely, the interaction between phases, such as solid particles and interstitial water in a saturated soil, like a saturated flow-like landslide, can be tracked through the *two-phase single-point* formulation (Jassim et al., 2013; Ceccato et al., 2018). In this case, the liquid and the solid acceleration fields ($\mathbf{a}_S - \mathbf{a}_L$ formulation) are the primary unknowns (Fern et al., 2019). Here, the flow and barrier are modelled, respectively, through the *two-phase* and the *one-phase* MPM formulations, whose details are reported in the Appendix 1. It is worth noting that the stress update strategy chosen is the "update stress last" (Fern et al., 2019) and for the velocity update the scheme of Sulsky et al. (1995) has been used (see also Fei et al., 2021). More details are available in the literature (Al-Kafaji, 2013; Martinelli and Galavi, 2021, 2022).

For the case of a barrier unfixed to the ground, the frictional resistance along the base is set equal to the 80% of the strength properties of the base material (Cuomo et al., 2020b). However, simulating deformable moving structures such as these barriers is not an easy task. In the current MPM code here used (Martinelli and Galavi, 2022), the mesh is moved during the simulation to keep the same contact nodes around the retaining structure. The reason is to increase the accuracy of the contact algorithm. This approach uses the moving-mesh concept, originally developed to model penetration of piles into the soil (Al-Kafaji, 2013). An advantage of this procedure is that the mesh can be refined around the structure and hence the refined area will always remain around the contact surface throughout the entire numerical simulation. This approach has been widely applied and validated in the Anura3D code, for quasistatic problems (see for instance the work of Ceccato et al., 2016; Ghasemi et al., 2018; Martinelli and Galavi, 2021 for what concerns CPT simulations) and for dynamic applications (see for instance the work of Galavi et al. (2019) for the simulation of impact-driven open-ended piles modelled as rigid body, and the work of Zambrano-Cruzatty and Yerro (2020) where the free-fall penetrometer is modelled both as a flexible and rigid object). Here, the barrier is assumed as rigid, and again the "moving mesh" has been used.

The contact between different bodies (flow-base, flow-barrier) is handle with a frictional contact algorithm. An improved contact algorithm was used, proposed by Martinelli and Galavi (2022), where the velocity of the liquid phase is corrected to prevent both inflow and outflow through the contact. Moreover, the computational scheme

Table 1
Mechanical properties.

Flow-like landslide											Barrier		
ρ_m (kg/m^3)	ρ_s (kg/m^3)	n (−)	K_0(−)	φ' (°)	c' (kPa)	E' (MPa)	ν (−)	k_{sat} (m/s)	μ_L (Pas)	K_L (MPa)	ρ (kg/m^3)	tan(δ) (−)	tan(δ_b) (−)
1800	1300	0.5	0.66	20	0	2	0.25	10^{-4}	10^{-3}	30	2000	0.29	0.29

Table 2
Geometric features for different scenarios.

ID	L_1 (m)	L_m (m)	i (−)	h (m)	V_1 (m^3/m)	$v_{0,1}$ (m/s)	β (°)	d (m)	L_2 (m)	B (m)	b (m)	H (m)
1	21.00	15.00	3	3.00	45.00	10	60	3.00	6.95	11.00	4.00	6.00
2	21.00	15.00	3	3.00	45.00	20	60	3.00	6.95	11.00	4.00	6.00
3	21.00	15.00	3	3.00	45.00	10	80	3.00	6.08	8.50	6.50	6.00
4	21.00	15.00	3	3.00	45.00	10	72	3.00	7.87	8.38	3.63	7.50
5	21.00	15.00	3	3.00	45.00	10	90	3.00	∞	–	–	∞
6	47.00	45.00	43	1.00	45.00	10	60	3.00	6.95	11.00	4.00	6.00

Table 3
Expected impact mechanism.

ID	Fr (−)	H/h(−)	Impact mechanism*
1–3	1.84	2.0	Standing jump
4	1.84	2.5	Standing jump
5	1.84	∞	Bores
6	2.76	6	Bores
2	3.69	2.0	Airborne jets

* from the application of the diagram proposed by Faug (2015)

proposed by Martinelli and Galavi (2022) is adopted to compute accurate reaction forces along contact surfaces, especially between non-porous structures and soils with high liquid pressures. The readers may find more details in Martinelli and Galavi, 2022.

The flow-like landslide is schematized as a saturated mixture with initial linear vertical distribution of pore-water pressure. The accurate spatial distribution of the pore-water pressure inside the landslide at the impact is important to consider. However, for the time being, we are only capable to start from a simplified distribution of pore-water pressure, that is hydrostatic along each vertical. As for the previous three landslide factors (shape, velocity, and thickness), the distribution of pore-water pressure changes during the impact process, at an extent depending on landslide volume and velocity, as well as in relation to the type and features of the barrier.

A non-associative (zero dilatancy) elasto-plastic Mohr-Coulomb behaviour is assumed for the saturated flow mass, whose mechanical properties and friction angle at the contact with the barrier are reported in Table 1. When the landslide impacts the barrier, it is a highly dissipative and transient phenomenon, which may include porosity changes because of consolidation and dilation. However, Cuomo et al. (2021a) have shown that the high mobility of flow-like landslides prevents a large change in porosity inside the landslide body. In fact, the impacting material is more prone to runaway than to be compressed behind the barrier. This reasoning applies to the whole landslide body, with some potential compression zones limited for instance to the dead zone behind the barrier.

Here, it is worth mentioning that the above MPM model has been formerly calibrated and validated through physical model tests, in particular flume and centrifuge tests, as reported by Cuomo et al. (2021a) and Di Perna et al. (2022). Other validations of the MPM model have been also proposed: for instance, Cuomo et al. (2020a) reproduced laboratory results of masonry walls tested under external out-of-plane loads; Cuomo et al. (2021b) validated the MPM model for a real landslide evolved into a flow. Thus, the capability for MPM-based modelling to reproduce the landslide-structure interaction has been ascertained before. Then, the same approach has been extended in this paper to the analysis of some of those landslide-structure interaction mechanisms to calibrate the proposed analytical method.

2.3. Parametric analysis of realistic scenarios

The complexity of the LSI has been explored through MPM (Di Perna, 2022), with reference to the effect of the ratio H/h, the slope β of the impacted side of the barrier, the bottom constraint for the barrier (fixed/unfixed). The geometric features of both the landslide and the barrier are summarized in Table 1, also considering different impact scenarios. Although simplified, the scheme resembles the main landslide characteristics such as velocity, impact height, non-zero interstitial pressures, with a range of geometric cases shown in Table 2. It is worth noting that the case of an infinite barrier is that considered in the literature empirical models (Armanini et al., 2011; Cui et al., 2015). The computational unstructured mesh is made of triangular 3-noded elements (for instance, 20,515 in the case 1 of Table 2) with dimensions ranging from 0.20 to 1.00 m for all the cases considered. Such mesh size was checked to be enough accurate to simulate the LSI mechanisms here investigated and it still allowed reasonable computational times for each simulation in the range of a few hours with a standard desktop computer.

The so-called phase diagram proposed by Faug (2015) for flow-structure interaction in the case of dry granular materials is here used for a preliminary assessment of the expected impact mechanisms (Table 3). However, for the saturated flows explored in this study, it might be not so convincing that this diagram is used directly. And, in fact the numerical model is later referred to confirm such preliminary assessment.

Some selected sets of the numerical results are reported to show the spatial distribution of pore-water pressure at different time lapses of the propagation stage (Figs. 4–6) for the different schemes of Table 1.

During the impact, the initial liquid pressure ($<30\ kPa$) changes over time, with the maximum value in the first instants of the impact process ($t = 1\ s$) and later diminishing down to nil in some cases. However, the maximum of pore-water pressure ($p_{L,\ max}$) reaches different values depending on the type of barrier. In fact, comparing an infinite vertical barrier (Fig. 4a) with a smaller (even fixed to the ground) trapezoidal barrier (Fig. 4b), it arises that $p_{L,\ max}$ is higher in the first case, since the overtopping is not allowed and so the impacted area of the barrier is larger than for the second case ($t = 1\ s$). At $t = 2\ s$, the flow overtops the smaller barrier (Fig. 4a) or goes beyond the barrier forming a prolonged jet (Fig. 4b). Liquid pressure is decreasing, indicating that we are in the decay zone of the impact force diagram. Subsequently ($4\ s < t < 6\ s$), the flow loses more and more energy and falls downwards (similarly, in both

Table 4
Selected parameters for validation of the analytical model through MPM simulations.

	Flow type landslide				Barrier	
	n (−)	h (m)	V_1 (m^3/m)	$v_{1,0}$ (m/s)	$m_2/m_1{}^{(*)}$ (−)	β (°)
Set I	0.3	3	45 ($i = 3$)	10	0.94	60
Set Iia	0.5	3	45 ($i = 3$)	15	1.10	60
Set Iib	0.5	3	45 ($i = 3$)	20	1.10	60
Set III	0.5	3	63 ($i = 5$)	10	0.80	60
Set IV	0.5	3	45 ($i = 3$)	10	1.10	80
Set V	0.5	4	48 ($i = 1$)	10	0.73	60

$^{(*)}m_2/m_1 \rightarrow \infty$ for fixed barriers

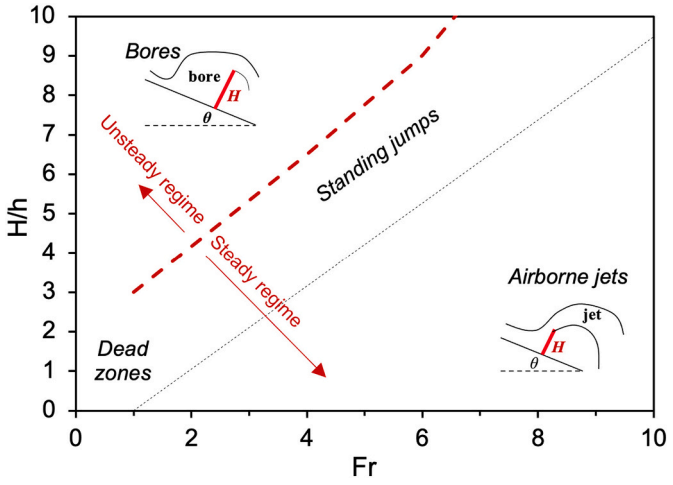

Fig. 1. Interaction diagram for a flow impacting a barrier (adapted from Faug, 2015).

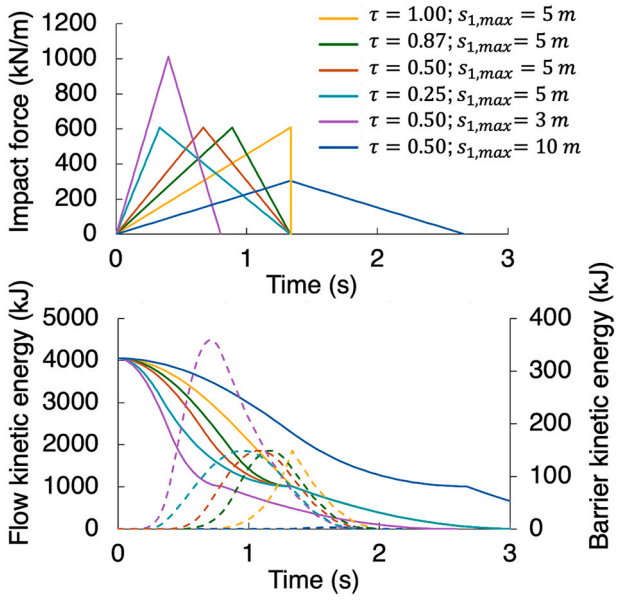

Fig. 9. Variation of impact forces and kinetic energy of the flow (solid lines) and the barrier (dashed lines), as schematised in the analytical model.

cases). The expected impact mechanism, as assessed from the diagram of Faug (2015), is confirmed in both the cases. For the infinite vertical barrier, a granular jump (named "bore") is formed which goes upstream of the barrier. For the embankment barrier, the impact mechanism is the standing jump, which is similar to the bores regime but here a part of the incoming flow is able to overtop the barrier, forming a jet with very low energy.

Several types of unfixed trapezoidal barriers have been considered to investigate different impact scenarios. Specifically, if the barrier is unfixed to the base ground, the maximum pore-water pressure $p_{L,\,max}$ at impact is of 11% lower than for a fixed barrier, because the sliding of the barrier hinders the building-up of water pressures inside the landslide. This is well captured by comparing Fig. 4b with Fig. 5a. Even if the impact mechanism is practically the same (standing jump), the amount of flow that propagates beyond the barrier is less for an unfixed barrier.

This outcome confirms previous research results showing that an increase in pore-water pressure favours the overtopping of a barrier (Song et al., 2017; Zhou et al., 2018). In addition, here the numerical MPM results also show that the inclination β and the barrier height relative to the flow depth (H/h) play a significant role in the generation of excess pore-water pressure inside the landslide body. Other insights are reported in Fig. 5a: a higher barrier (Fig. 5b) makes a reduction of $p_{L,\,max}$ from 135 kPa to 123 kPa; while a more inclined impact side (Fig. 5c) gives a higher value equal to 146 kPa. However, all these values are always lower than the case of a fixed barrier. The type of impact mechanism is a standing jump for all the scenarios, but the amount of material that is retained by the barrier ($V_{f,\,sx}$) increases with the inclination β and height H of the barrier. The final displacement exhibited by the barrier is larger when the inclination β increases and for a smaller base of the barrier itself.

Different flows are also considered to investigate other impact mechanisms (Fig. 6). A higher flow velocity (Fig. 6a) than for the case of Fig. 5a produces an increase of $p_{L,\,max}$ from 135 kPa to 172 kPa. The expected impact mechanism is an airborne jet (Table 3) and it is confirmed by the numerical simulation. A very prolonged jet with high energy is formed during the impact thus the amount of material that is retained by the barrier is quite smaller than the standing jump cases. Completely different is the case of a thinner flow-like landslide (Fig. 6b), where the flow hits the barrier and propagates upstream of it in unsteady conditions (bores regime). The flow has a very low kinetic energy and so the potential prevails, not allowing the flow to overtop the barrier. Also in this case, the link between pore-water pressure at impact and the overcoming material is confirmed.

The MPM numerical simulations allow investigating the landslide-structure interaction from both a dynamic and kinematic point of view. It is worth noting that different materials and differently idealized impact conditions are here considered through different MPM formulations. Particularly, the *one-phase single point* formulation is used for modelling a dry granular flow and a saturated flow under undrained conditions, while the *two-phase single point* formulation is used for the other cases. As shown in Fig. 7, the peak of the horizontal impact force $F_{2,\,x}$ is quite similar for all the cases, apart from case 3 that has the highest value due to the larger impacted area and from case 6 that does not show a peak at the impact moment. The latter trend is typical for impact mechanisms which are not characterized by the formation of a jet. The horizontal force of a one-phase flow differs from the two-phase coupled cases for $t > 2s$. This means that the presence of a liquid phase inside the flow generates a longer interaction with the barrier due to the build-up of excess pore pressure.

In contrast, the vertical component $F_{2,\,y}$ has a different trend for each impact scenario, reaching the lowest values for the inclination $\beta = 80^{\circ}$ (case 3). This happens because the vertical component of the impact force is strictly linked to the weight of the flow that propagates beyond the barrier. For this reason, the vertical impact force plays an important role in the prediction of the barrier maximum displacement, which increases when the vertical force approaches to zero. The undrained simulation is characterized by the maximum values of pore pressure within the flow and therefore the more mass overrides the barrier because of the impetus of the flowing mass, the higher the vertical force generated.

The temporal variation of the forces F_3 and F_4 are also obtained. The

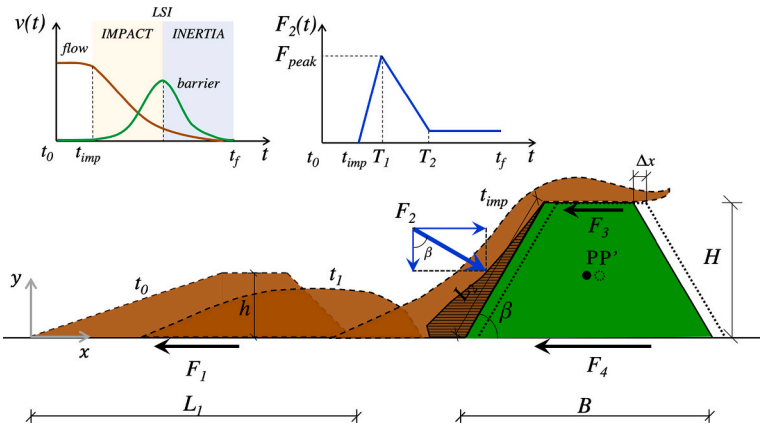

Fig. 2. Conceptual scheme for Landslide-Structure Interaction (LSI).

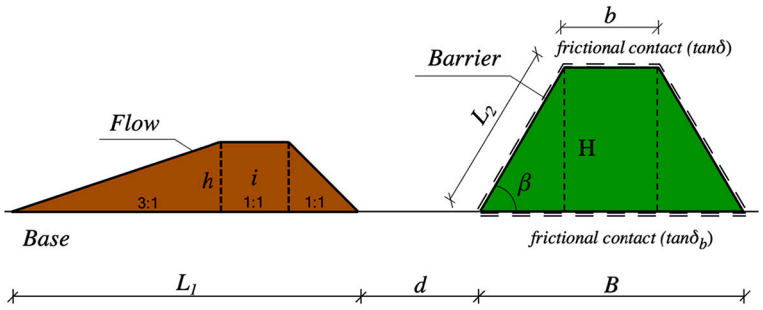

Fig. 3. Geometric schematization of the problem in the numerical model.

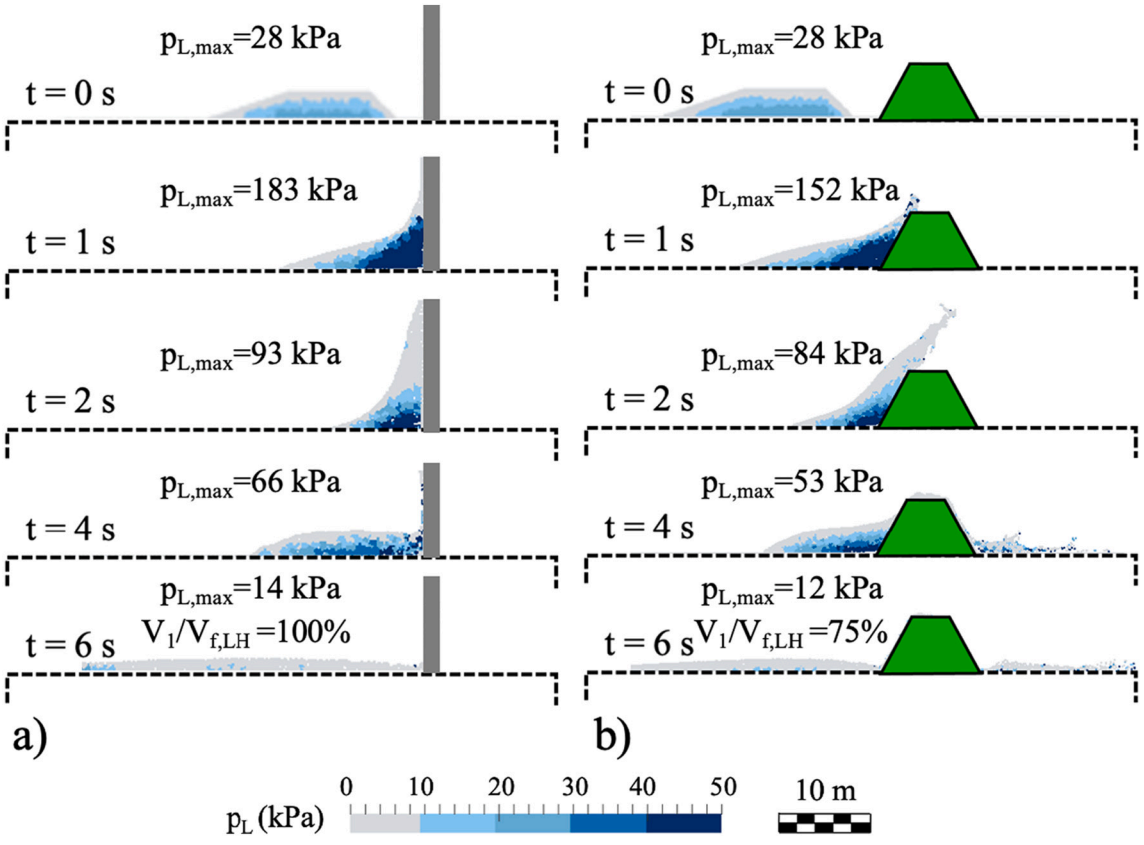

Fig. 4. Pore-water pressure distribution for: (a) infinite barrier (case 5); (b) fixed artificial barrier (case 1).

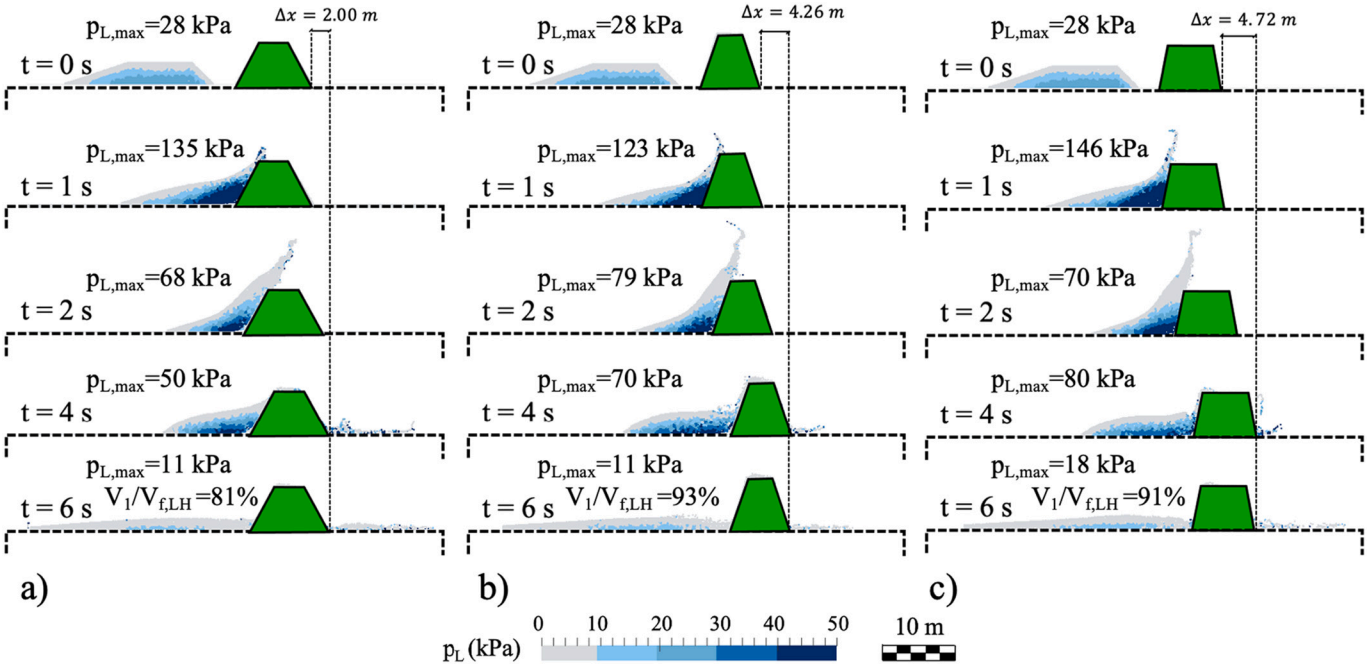

Fig. 5. Pore-water pressure distribution for various unfixed artificial barriers: (a) H/h = 2; β = 60° (case 1); (b) H/h = 2.5; β = 72° (case 4); (c) H/h = 2; β = 80° (case 3).

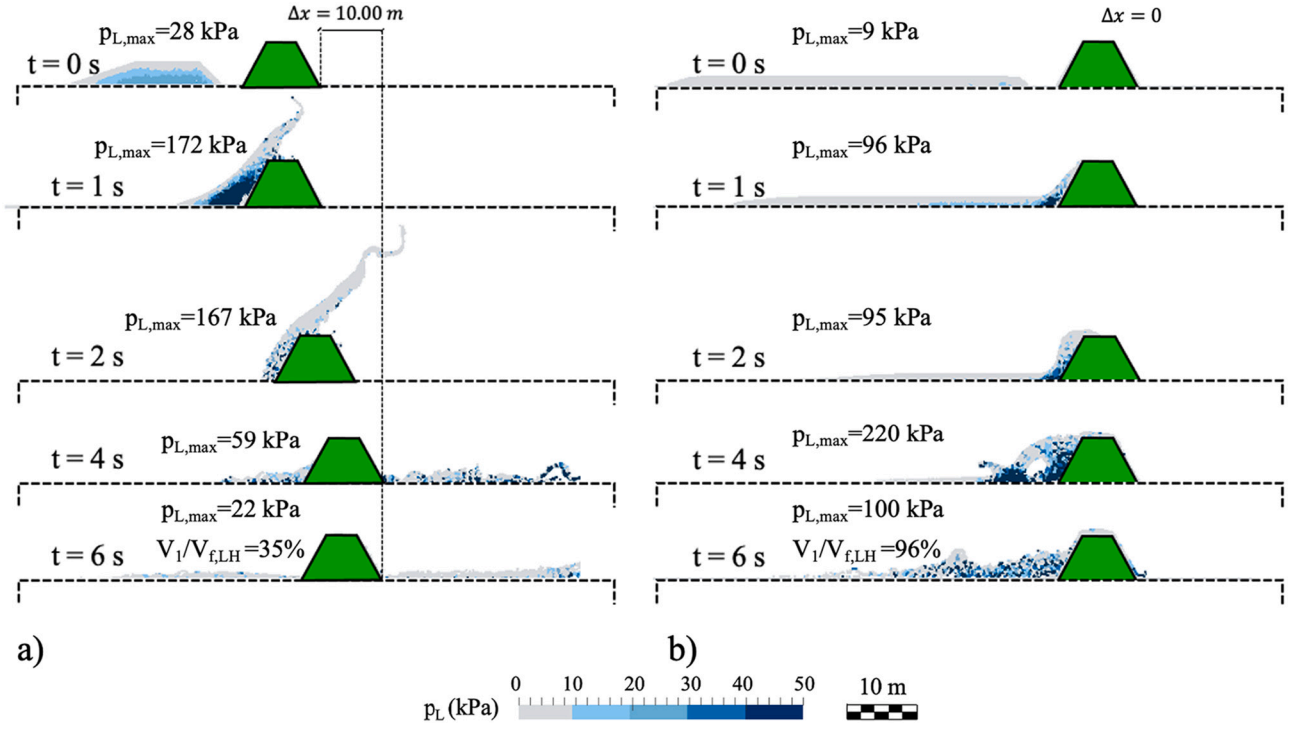

Fig. 6. Pore-water pressure distribution for different flows impacting unfixed artificial barriers: (a) H/h = 2; v_0 = 20 m/s (case 2); (b) H/h = 6; v_0 = 10 m/s (case 6).

frictional force above the barrier F_3 is due to the barrier overtopping by the flow and so it depends on the amount of flow that goes beyond the barrier. In fact, the highest value of F_3 is reached for the case 1, where the retained volume is the smallest one simulated. This force can also have sign changes (case 4) when the flow, instead of going beyond the barrier, falls within the volume retained by the barrier. However, the force F_3 can be neglected if compared to the frictional force at the base of the barrier F_4.

For the sake of simplicity, the flow basal frictional force F_1 is assumed as nil in all the cases through a smooth contact not to influence the flow height and velocity at impact.

The kinetic energy of the incoming flow (in solid lines) has a quite similar trend for most of the moving barrier scenarios. All curves show a sudden reduction up to $t \cong 2\ s$, that is the moment from which the formed jet takes the downward direction. This means that energy is transforming from kinetic to potential. Furthermore, the decay is faster

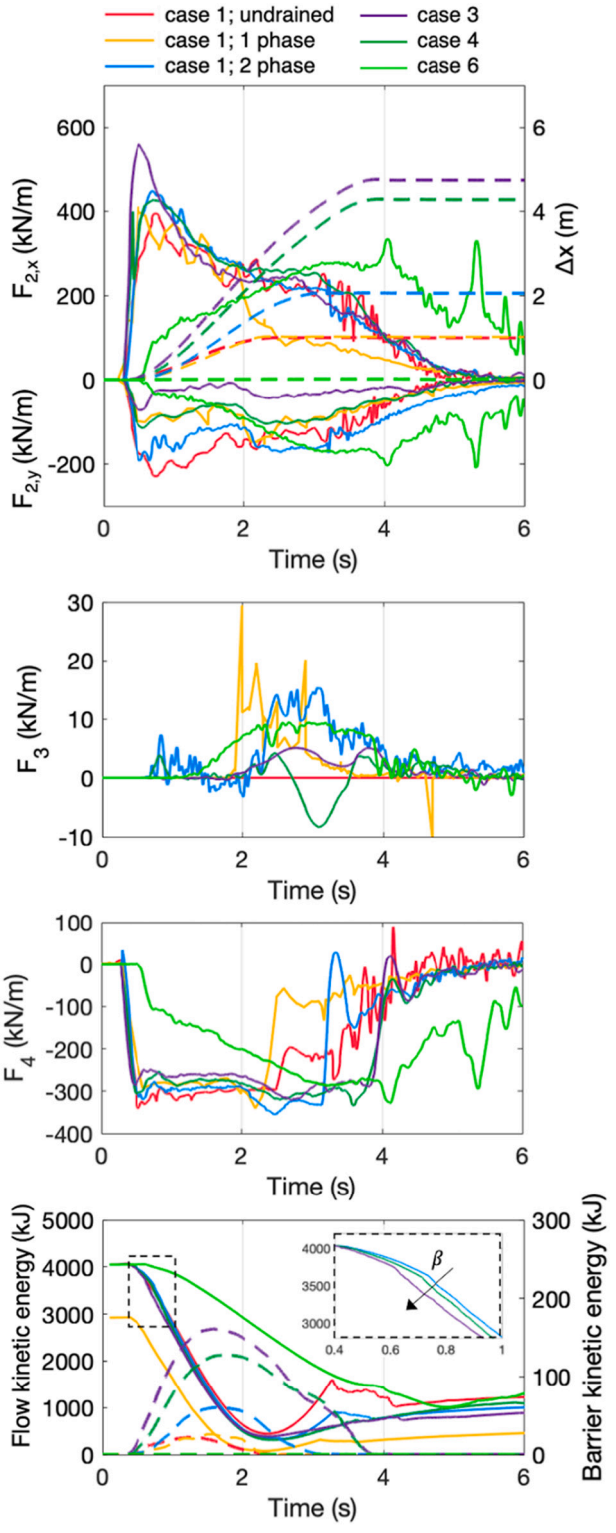

Fig. 7. Impact forces (solid lines) and barrier displacements (dashed lines) and kinetic energy of the flow (solid lines) and the barrier (dashed lines) in different scenarios.

for greater inclinations β, due to the increasing in kinetic energy of the barrier (in dashed lines), and therefore more flow kinetic energy is transformed into work produced by the movement of the barrier. Different is the kinetic energy evolution for the case 6, where the reduction is slower and quite constant over time without showing any secondary peaks as a jet is not formed.

The kinetic energy for the dry flow assumes the lowest values compared to the saturated flow scenarios and thus also the kinetic energy of the barrier, due to the more contained movement. This suggest that the presence of a liquid phase inside the flow makes the interaction with the barrier more dramatic. If the landslide-structure interaction is studied in undrained conditions the flow kinetic energy is slightly higher than the cases with hydro-mechanical coupling until $t \cong 2\,s$. Afterwards, the difference becomes more evident because the jet is faster and more elongated and so more mass exceeds the barrier, leading to higher kinetic energy of the jet.

However, there are still some limitations of the current MPM modelling. For example, more sophisticated constitutive models for the flowing mass could be investigated, even considering the presence of viscous stresses inside the flow. The selection of an appropriate constitutive model is one key to having successful simulations. Moreover, the assumption of rigid barrier used for the design of DGRBs is acceptable for the sake of safety, but it can lead to oversized structures. More sophisticated analyses are needed for analysing (i) the large and irreversible deformations induced, (ii) the nonlinear soil stress-strain behaviour, and (iii) the interaction between the different components (reinforcement elements and backfill soil). These limitations must be overcome in the future, expanding the research to new frontiers.

3. Casting a novel analytical model for LSI

3.1. Formulation

An analytical model (Di Perna, 2022) is set up where the landslide body and the barrier are considered as two colliding bodies (Fig. 8a). The approaching flow is schematized as a box of volume V_1, with mass m_1, length $L_{1,\,0}$, depth h, unitary width, density ρ_m, and initial velocity $v_{1,\,0}$. The barrier is rigid, with its own mass m_2 and it is free to slide along the base. The frictional contact at the base is equal to $\tan(\delta_b)$, which is set as the 80% of the strength properties of the subsoil base material (Cuomo et al., 2020b).

The case of a fixed barrier is also possibly considered, setting the mass of the barrier to a very high value compared to that of the flow (i.e., $m_2/m_1 \rightarrow \infty$).

The interaction between the landslide and the barrier (*impact* stage) is schematized by an inelastic collision (Fig. 8b), therefore after the impact the two bodies reach the same velocity v_{CM}, applied in the centre of mass (*CM*) of the system. The impact force F is a spatio-temporal function since the approaching volume of the landslide increases with time until T_1 and then diminishes due to the dissipation of flow energy. The quantity s_1 represents the change (shortening) in landslide body after the impact and it is computed as positive in the direction opposite to the flow movement. Being the impacting mass saturated, the expected behaviour is that a part of the landslide mass will overtop the barrier and the remaining volume will interact with the barrier. The maximum value $s_{1,\,max}$ is reached when the impact force is equal to the peak value. This means that only a part of the total volume of the landslide contributes to the interaction with the barrier. Once the interacting volume (hs_1) has contributed to increase the impact force, it may overtop the barrier creating a vertical jet or may be completely reflected. If a vertical jet is formed, supposing that all the interacting volume has overtopped the barrier for the sake of safety, the amount of flow mass that can be found beyond the barrier will be at most equal to the $\rho_m hs_{1,\,max}$. After reaching the maximum impact pressure, the flow mass decelerates and the interacting volume decreases in time until nil, i.e., $s_1 = 0$ at $t = T_2$. During the interaction, the barrier can slide along its base of a quantity equal to Δx.

The proposed analytical model reproduces the global behaviour of landslide body in the *LSI* process and implicitly disregards some local mechanisms, such as the formation of a dead zone, over which the rear part of the landslide body propagates (Ng et al., 2018). This is one limitation of the model.

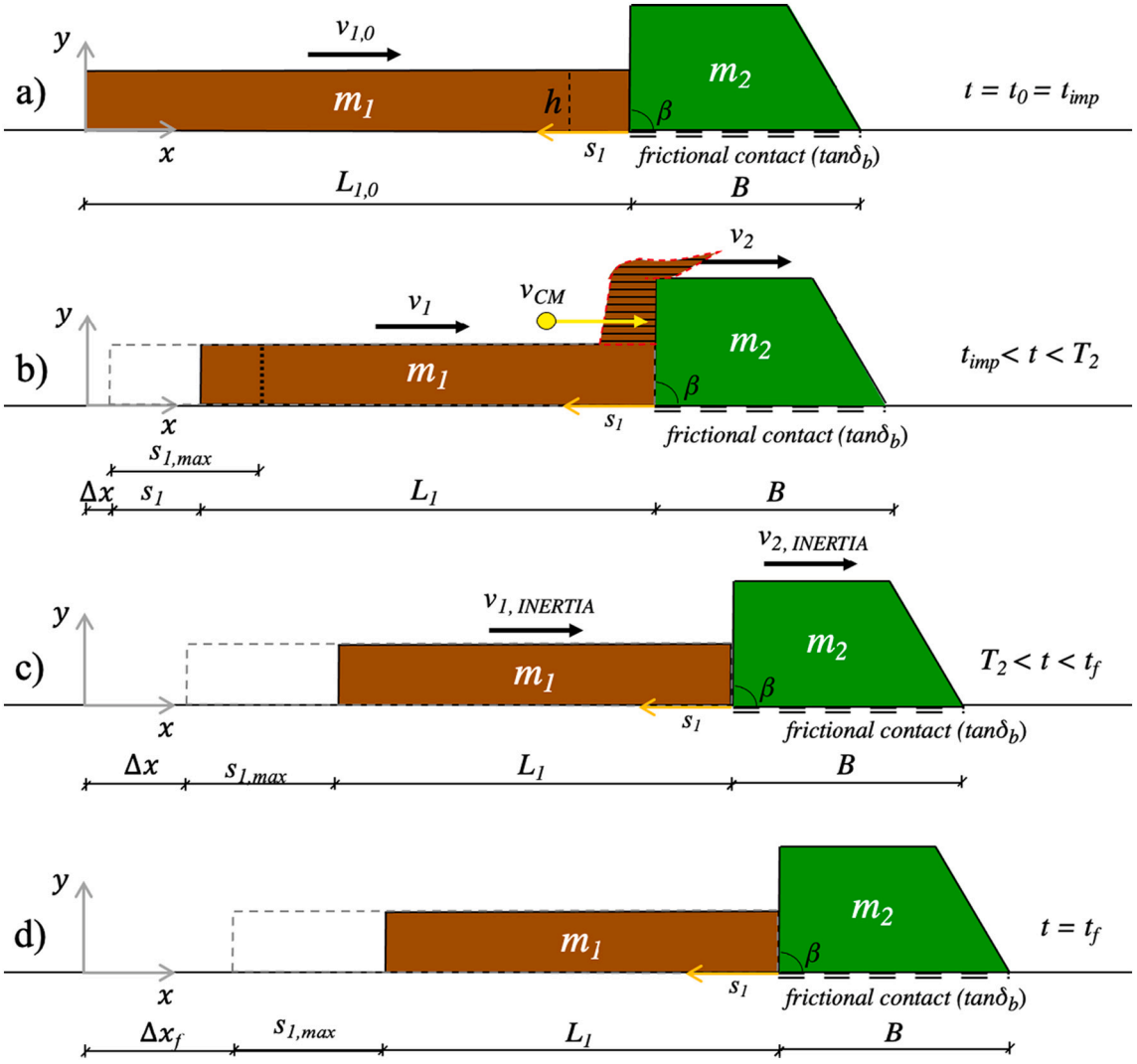

Fig. 8. Conceptual scheme in the analytical model: (a) at the early stage of impact, (b) during the impact, (c) during the inertial phase, d) at final condition.

At the end of the *impact* stage, the motion of the system is governed by the inertial forces and the length s_1 is assumed to be zero (Fig. 8c). Due to friction, both the colliding bodies decelerate so that their velocity ($v_{INERTIA}$) decreases over time. The final configuration (Fig. 8d) is reached when the two bodies are completely stopped and have travelled for a total distance of Δx_f.

For the action-reaction principle, the mutual impact forces of body 1 (i.e., the landslide mass) and body 2 (i.e., the barrier) are equal and opposite. Under the assumption of inelastic collision, the quantities referred to body 1 are considered and the governing equations obtained. Doing so, the trend of F along s is assumed to be less than linear (Eq. (5)), because this assumption considers the fact once the interaction has started, the additional volumes interacting with the barrier generate smaller and smaller increases in impact pressure with time.

The impact force trend $F(t)$ in Eq. (6) can be obtained from Eq. (5) by introducing the formulation of $s_1(t)$ reported in Appendix 2 (Eq. (A23)).

It is worth noting that the quantity $K_1 = \left(\frac{m_1 m_2}{m_1+m_2}\right) \bullet \left(\frac{v_{1,0}-v_{2,0}}{s_{1,max}}\right)$ is a model parameters referred to the body 1, while the quantities q_1 (Eq. (7)) and T_2 (Eq. (8)) are the model primary unknows. Once known both T_2 and T_1 (Eq. (16)), that can be achieved by fixing the ratio $\tau = T_1/T_2$ (for example from experimental evidence), the description of the impact dynamics is complete. To consider this more realistic trend, the peak time T_1 can be achieved by fixing the ratio $\tau = T_1/T_2$ (for example from experimental evidence), as reported in Eq. (9).

The mathematical steps are reported in Appendix 2, while the main equations are reported below. The model parameters that must be appropriately individuated are $s_{1,\ max}$ and τ.

$$F(s) = q_1 \sqrt{s_1} \tag{5}$$

$$F(t) = \frac{1}{2}\frac{{q_1}^2}{K_1} t \tag{6}$$

$$q_1 = \frac{3}{4}\frac{K_1\left(v_{1,0}-v_{2,0}\right)}{\sqrt{s_{1,max}}} \tag{7}$$

$$T_2 = \frac{8}{3}\frac{s_{1,max}}{\left(v_{1,0}-v_{2,0}\right)} \tag{8}$$

$$T_1 = \tau T_2 \tag{9}$$

The kinematics of the landslide during impact is described by the velocity of its centre of mass (Eq. (10)) and kinetic energy (Eq. (11)). Similar equations are derived for the body 2 (i.e the barrier). Here, the frictional contact along the base of the barrier causes its deceleration and therefore it must be considered in the velocity formulation (Eq. (12)). The deceleration is equal to the ratio between the frictional contact force and the mass of the barrier and remains constant during the interaction with the flow. The formulations derived for the velocity,

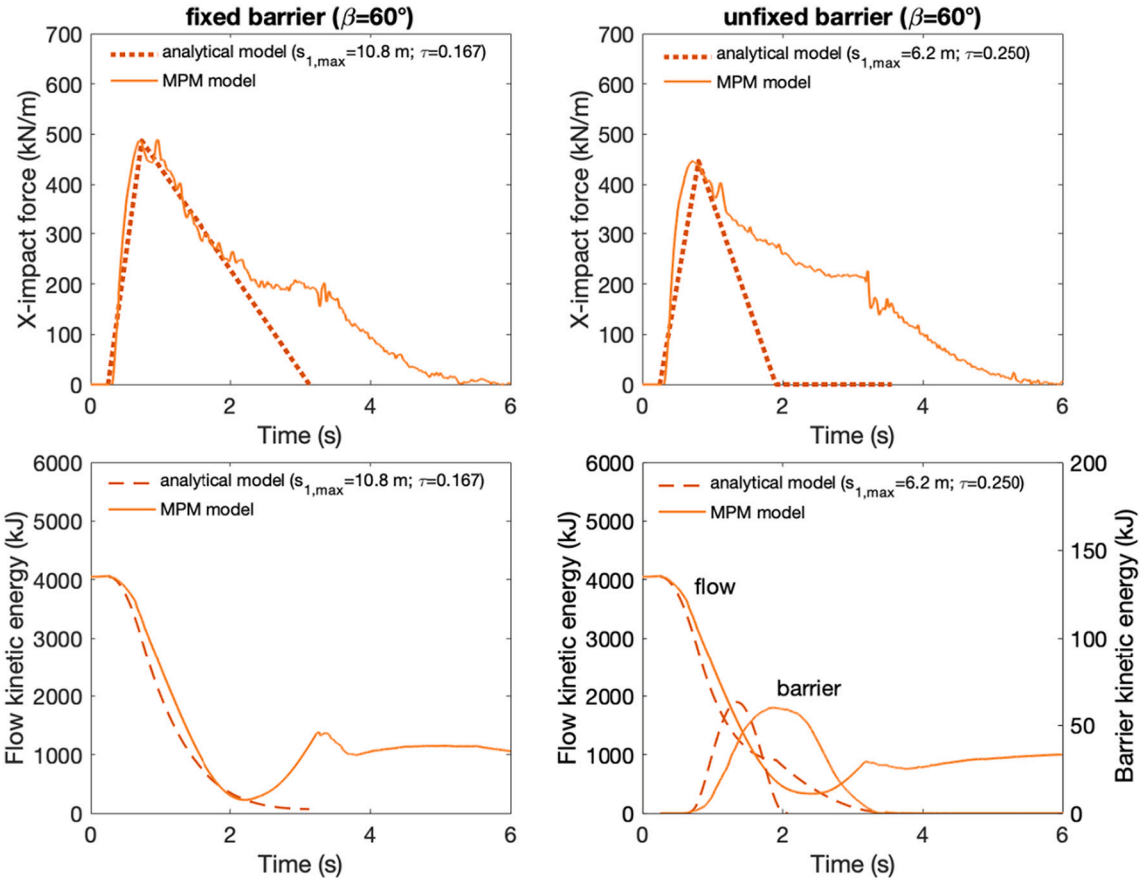

Fig. 10. Example of the analytical model calibration through MPM simulations (case 1 in Table 1).

kinetic energy and displacements of the barrier are reported in Eqs. (12)–(14), respectively.

$$v_1(t) = v_{1,0} - \frac{q_1^2}{4K_1 m_1} t^2 \tag{10}$$

$$E_{k,1}(t) = \frac{1}{2} m_1 v_1^2(t) \tag{11}$$

$$v_2(t) = v_{2,0} - g tan(\delta_b) t + \frac{q_2^2}{4K_2 m_2} t^2 \tag{12}$$

$$E_{k,2}(t) = \frac{1}{2} m_2 v_2^2(t) \tag{13}$$

$$\Delta x(t) = v_{2,0} - \frac{g}{2} tan(\delta_b) t^2 + \frac{q_2^2}{12K_2 m_2} t^3 \tag{14}$$

After the impact, the landslide-structure interaction between the two bodies can be neglected since the motion is mostly governed by the friction at the base. In this stage, the change in velocity over time (Eq. (15)) can be calculated referring to the uniformly decelerated motion equations. The final displacement Δx_f of the barrier (Fig. 8d) is reported in Eq. (16).

$$v_{INERTIA}(t) = v_{CM} - \left|a_{fr}\right| \Delta t = v_{CM} - g\ tan(\delta_b)\ (t - T_2) \tag{15}$$

$$\Delta x_f = \frac{{v_{CM}}^2}{2g\ tan(\delta_b)} + v_{2,0} T_2 - \frac{g}{2} tan(\delta_b) {T_2}^2 + \frac{q_2^2}{12K_2 m_2} {T_2}^3 \tag{16}$$

In this analytical model two quantities $s_{1,\ max}$ and τ must be evaluated, and it is useful to understand the meaning of these variables in the assessment of both impact force and kinetic energy variation in time. Supposing that the two bodies have the same mass $m_1 = m_2 = 81000\ kg$, and $L_{1,\ 0} = 15\ m$; $h = 3\ m$; $\rho_m = 1800\ kg/m^3$; $v_{1,\ 0} = 10\ m/s$; $v_{2,\ 0} = 0\ m/s$; $\beta = 90^\circ$; $\tan\delta_b = 0.29$.

From the variation of impact forces, it emerges that the larger $s_{1,\ max}$ the lower the peak force value. Since the linear momentum is independent of $s_{1,\ max}$, the reduction of the flow velocity from $v_{1,\ 0}$ to v_{CM} occurs over a greater distance (as understandable from Eq. (A16) in Appendix 2). Hence, the impact time T_2 increases with higher values of $s_{1,\ max}$. This is also reflected in the computation of the kinetic energy over time, where for larger values of $s_{1,\ max}$ the flow energy reduction is more gradual. For the barrier, lower value of $s_{1,\ max}$ lead to higher peak of kinetic energy since the same amount of momentum is transferred from the flow to the barrier in a shorter time lapse. The change in τ also leads to different results as for $\tau \longrightarrow 1$ it occurs that $T_1 \longrightarrow T_2$. This also regulates the slope of the rise trend of the impact force diagram, being more inclined for lower values of T_1. The inclination of the rise period influences the kinetic energy trend being its variation more gradual when τ approaches unity.

3.2. Calibration

The proposed analytical model needs the calibration of the quantities $s_{1,\ max}$ and τ before being adopted for the prediction of landslide-structure interaction. These terms are obtained through Eq. (5). And Eq. (9), respectively, using the peak value of the horizontal impact force and peak time T_1 obtained from the MPM simulations. An example of the calibration for both fixed and unfixed barrier is reported in Fig. 10. Then, the trend over time of the kinetic energy is plotted for both the colliding bodies using the calibrated parameters. The results show a good correspondence between analytical and MPM model either in terms of impact forces or in terms of kinetic energy.

To quantify the confidence in the predictive capability of the model,

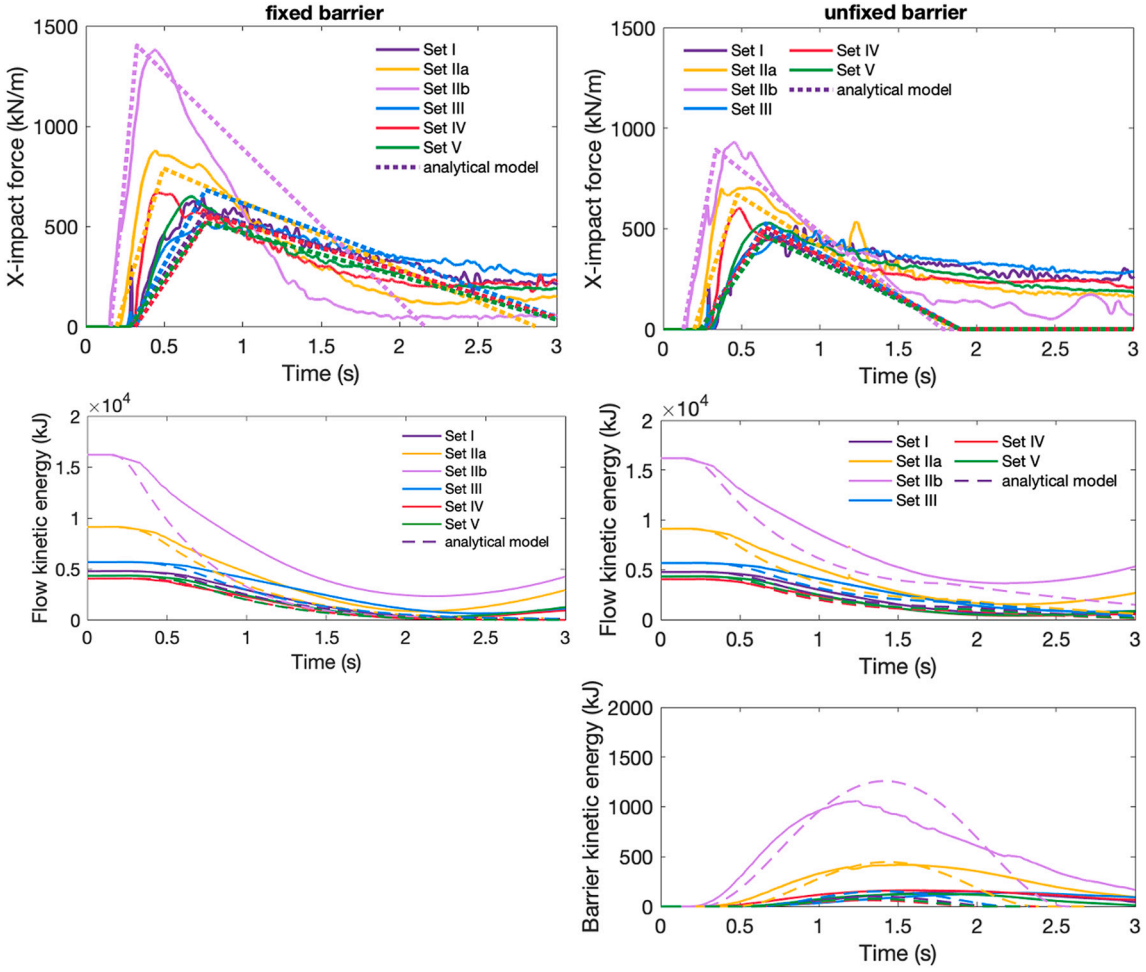

Fig. 11. Calibration results of the analytical model through MPM simulations (cases in Table 4).

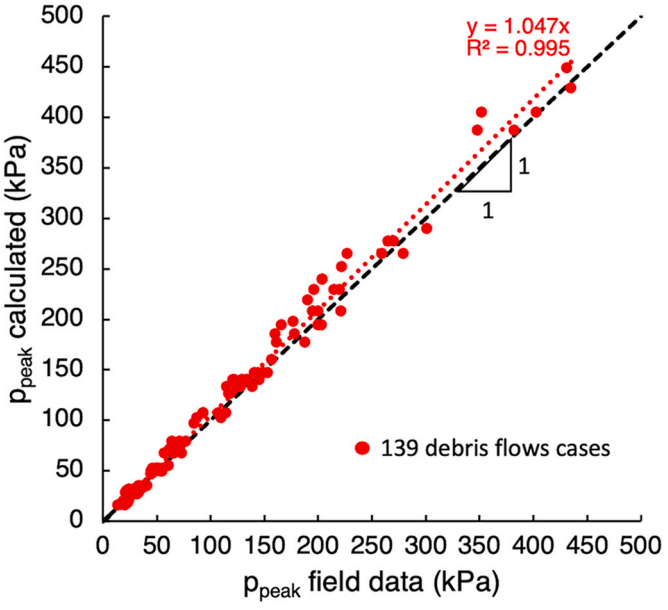

Fig. 12. Application of the proposed analytical model to the large field dataset (139 cases) collected by Hong et al. (2015).

a validation assessment is needed. The ratio $\lambda = s_{1,\,max}/L_{1,\,0}$ obtained from calibration (0.72 and 0.41 for fixed and unfixed barriers, respectively) was maintained unchanged and thus it was used to calculate the quantities $s_{1,\,max}$ for each impact scenario.

However, to obtain more precise results for identical flows with different velocities, the quantities $s_{1,\,max}$ and τ must be changed so that they are directly and indirectly proportional to the initial velocity $v_{1,\,0}$, respectively. This means that the ratio $v_{1,\,0}/s_{1,\,max}$ and the product $v_{1,\,0}\tau$ are kept constant. If it happens that $s_{1,\,max} > L_{1,\,0}$ then the assumption $s_{1,\,max} = L_{1,\,0}$ must be set.

Nevertheless, real case landslides have different volumes, density, impact height, etc. from each other thus estimating $s_{1,\,max}$ through the calibrated λ is the best solution.

The selected parameters used for assessing the goodness-of-fit for the analytical model under different scenarios are also here the porosity, the impact height, the triggered volume, the initial velocity of the landslide and the inclination of the impacted side of the barrier (Table 4).

The correspondence of the results is still good for all the calibration set (Fig. 11), where the analytical model can predict quite well the peak of the impact force and its time of occurrence. The trend over time of flow kinetic energy is traced in broad terms for both fixed and unfixed barriers. The barrier kinetic energy is reproduced quite well during the acceleration phase, but a little worse during the reduction phase since the interaction calculated with MPM lasts longer.

The analytical solution appears to overestimate the time of occurrence for case "set IV". In this case, the barrier front is 80° steep, while in the other cases is 60°. Of course, the inclination of the barrier side is important in the *LSI* process. However, the mismatch with numerical

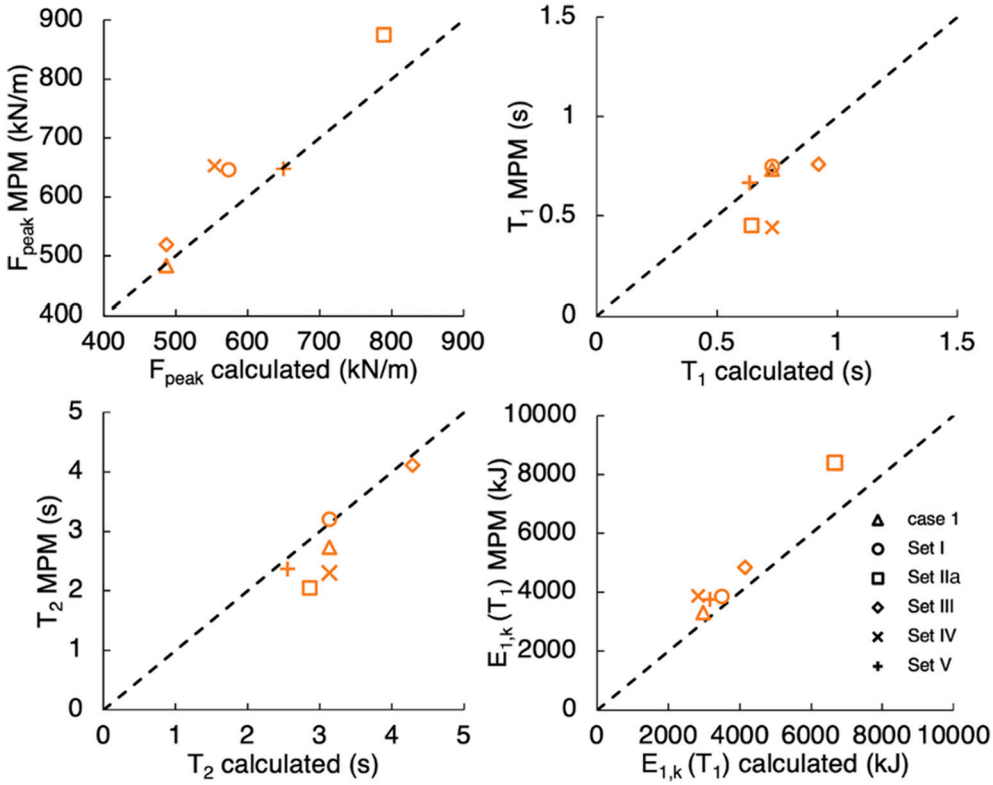

Fig. 13. Comparison of MPM and proposed analytical model for the cases of fixed barriers.

model outcomes is considered as negligible. It is also important noting that the (necessarily simplified) analytical model is proposed as a fast design tool. Of course, the solution(s) individuated through this new proposed analytical method must be carefully verified by means of 2D or 3D numerical (or physical) modelling.

Concerning that, we can observe that a variety of numerical methods was developed to simulate large-deformation problems and examples are listed in the introduction of the manuscript. A complete list of available methods is reported in Soga et al. (2016). On one hand, it is well-known that FEM has severe limitations in simulating problems with extreme deformations, which are caused by extreme element distortions (e.g., Soga et al., 2016). On the other hand, in this manuscript, MPM was used to simulate landslide-barrier interaction, which is a large-strain problem. The goal is not to highlight pros- and cons- of this method compared to others, but to use a validated MPM tool to calibrate analytical models which can be easily used in engineering practice.

3.3. Validation for a large dataset of field evidence

The proposed analytical model is validated to interpret a large dataset of real observations of flow-type landslides measured through a permanent monitoring station.

The field dataset from Hong et al. (2015) includes thickness, density, channel width, volume of discharge, velocity and impact forces recorded in real time during debris flow events.

The data are relative to 139 historical events that took place between 1961 and 2000 in the Jiangjia Ravine basin, located in the Dongchuan area of Yunnan Province in China (Zhang and Xiong, 1997; Kang et al., 2007; Hong et al., 2015). The bulk density ranges from 1600 to 2300 kg/m^3 with fluid concentration ranging from 0.15 to 0.6. The dataset is well suited for the validation purpose as it has a wide range of values: $v_{1,\,0} = 3 - 14\ m/s$, $h = 0.2 - 2.7\ m$, $V_1 = 269 - 1.75 \bullet 10^6\ m^3$ and $p_{peak} = 14 - 435\ kPa$.

The parameters needed to compute the impact pressure through the analytical model are K_1, q_1 (Eq. (7)) and $p_{peak} = q_1 \sqrt{s_{1,max}}/h$ (Eq. (5)). The quantity $s_{1,\,max}$ is calculated for each flow data as $\lambda L_{1,\,0}$, using the value $\lambda = 0.72$ calibrated in the case of fixed barriers. The flow length $L_{1,\,0}$ is obtained dividing the measured volume of discharge by the impact area (which is the product of the channel width and the flow thickness).

The validation results are reported in Fig. 12 and show a good correspondence with the field data. A slight overestimate is achieved especially for high impact pressures.

The application of the numerical MPM model is beyond the scope this paper, while it could be a future development of the research.

4. Discussion

A comparison between the presented models is necessary to assess their strengths and weaknesses in analysing landslide-structure interaction.

MPM is an advanced numerical method and has proved to be reliable in predicting the impact force trend over time (Cuomo et al., 2021a, 2021b). Moreover, unlike field evidence or laboratory tests, the numerical results provide additional features, through the computation and time-space tracking of different quantities, such as stress, strain, pore pressure, solid and liquid velocities, which cannot be easily monitored or obtained in the field.

Particularly focusing on LSI, MPM has many advantages. Primarily, it allows considering all such important aspects of the saturated flows, i.e., hydro-mechanical coupling and large deformations during propagation and impact. It was observed, in fact, that the presence of a liquid phase inside the flow can lead to different impact regimes in respect to dry granular flows, highlighting the importance of considering the solid-fluid interaction in the analyses. The accurate knowledge of the impact mechanism and so the evolution of flow depth and velocity is crucial for the design of mitigation countermeasures. For example, the accurate estimate of the length of the vertical jet must prevent that the retaining structure is overtopped by the flow, thus being ineffective. However,

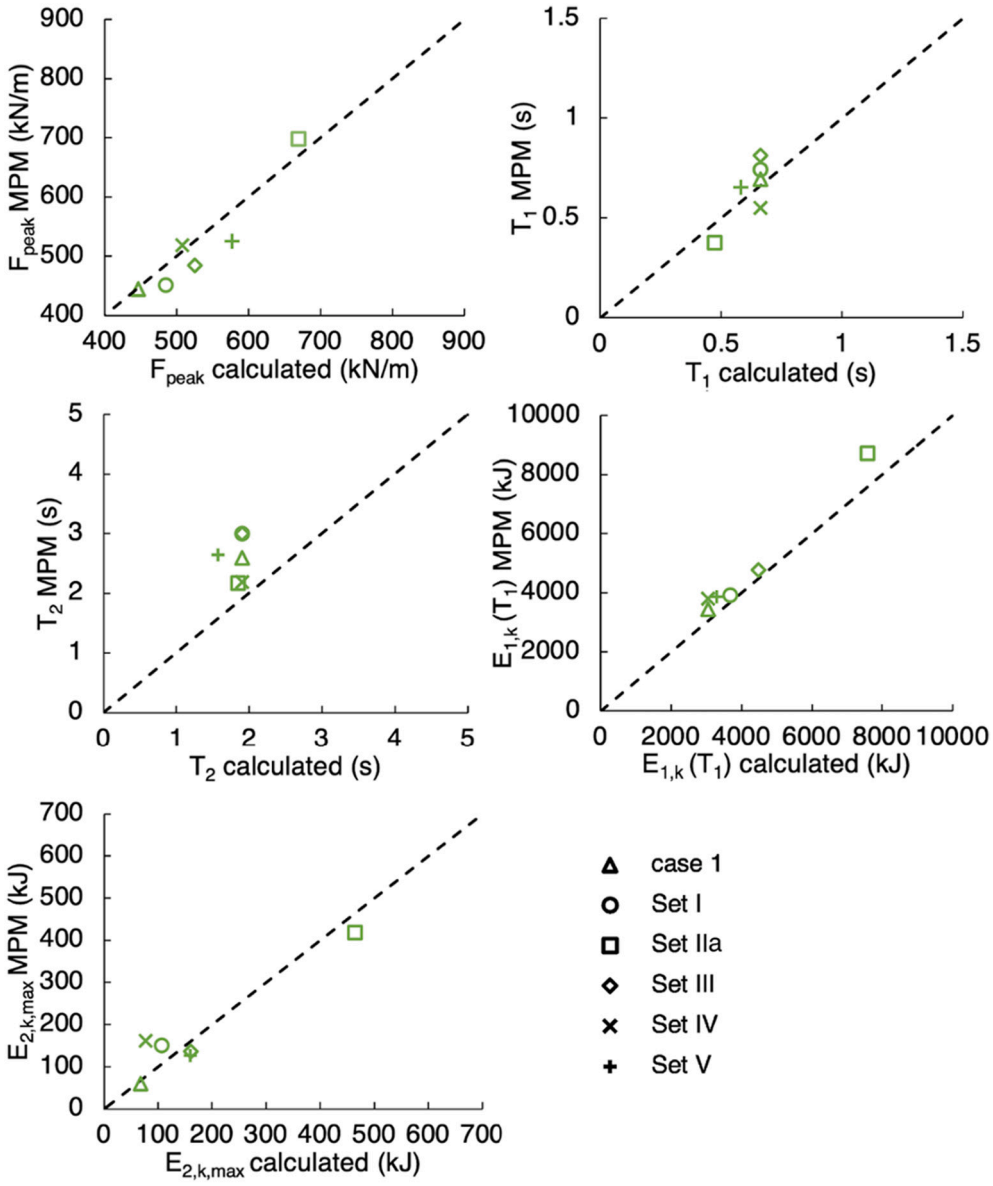

Fig. 14. Comparison of MPM and proposed analytical model for the cases of unfixed barriers.

MPM suffers from some limitations, such as the high computational cost and until now the difficulty of being available in engineering practice.

Analytical and empirical models are more immediate and easier to use than MPM, and thus they could be preferable in the assessment of the LSI problems for design purposes.

Considering the impact scenarios used in the above-mentioned analyses, Figs. 13–14 show the comparison between MPM and the proposed analytical model in evaluating the most representative quantities in an LSI analysis. It emerges a general agreement among the models, considering both fixed and unfixed barriers. Fig. 13 shows that the proposed analytical model for fixed artificial barriers predicts quite well the peak impact force with a slight underestimation in some cases. The other quantities (T_1, T_2 and $E_{k,\,1}(T_1)$) are also characterized by a good match, apart from Set IIa and Set IV that give an overestimation for T_1, T_2 and an underestimation of $E_{k,\,1}(T_1)$) indicating that the flow velocity and the inclination β are less predicted.

For unfixed barriers (Fig. 14), there is a high correspondence in terms of F_{peak}, T_1 and $E_{k,\,1}(T_1)$ for all the scenarios. Even the maximum kinetic energy of the barrier $E_{k,\,2,\,max}$ is predicted quite well, apart from Set I and Set IV where the MPM simulations gives higher results. This means that the porosity n and the inclination β are the most influential parameters when evaluating $E_{k,\,2,\,max}$ with the analytical model. About the time T_2 and the flow energy $E_{k,\,1}(T_1)$, the analytical solutions give an underestimation of the MPM results. This is mainly linked to the inability of this analytical model in considering the hydro-mechanical coupling and large deformations within the flow, which play a crucial role during the interaction with the barrier.

The proposed analytical model is finally compared to some empirical formulations available in the scientific literature (Fig. 15). The empirical models have been classified into three groups: (i) hydro-static models, which require only flow density and thickness for evaluating the maximum impact pressure; (ii) hydro-dynamic models, based on flow density and the square velocity of the flow; (iii) mixed models, that include both information about the static and the dynamic component of the flow. The latter group is preferable; thus, the chosen empirical formulations are all taken from group (iii): Hübl and Holzinger, 2003, Armanini et al. (2011), Cui et al. (2015), Vagnon (2020) and Di Perna et al. (2022).

The large dataset used for the comparison includes 139 debris flow cases (from Hong et al., 2015) already considered in paragraph 4.3. The

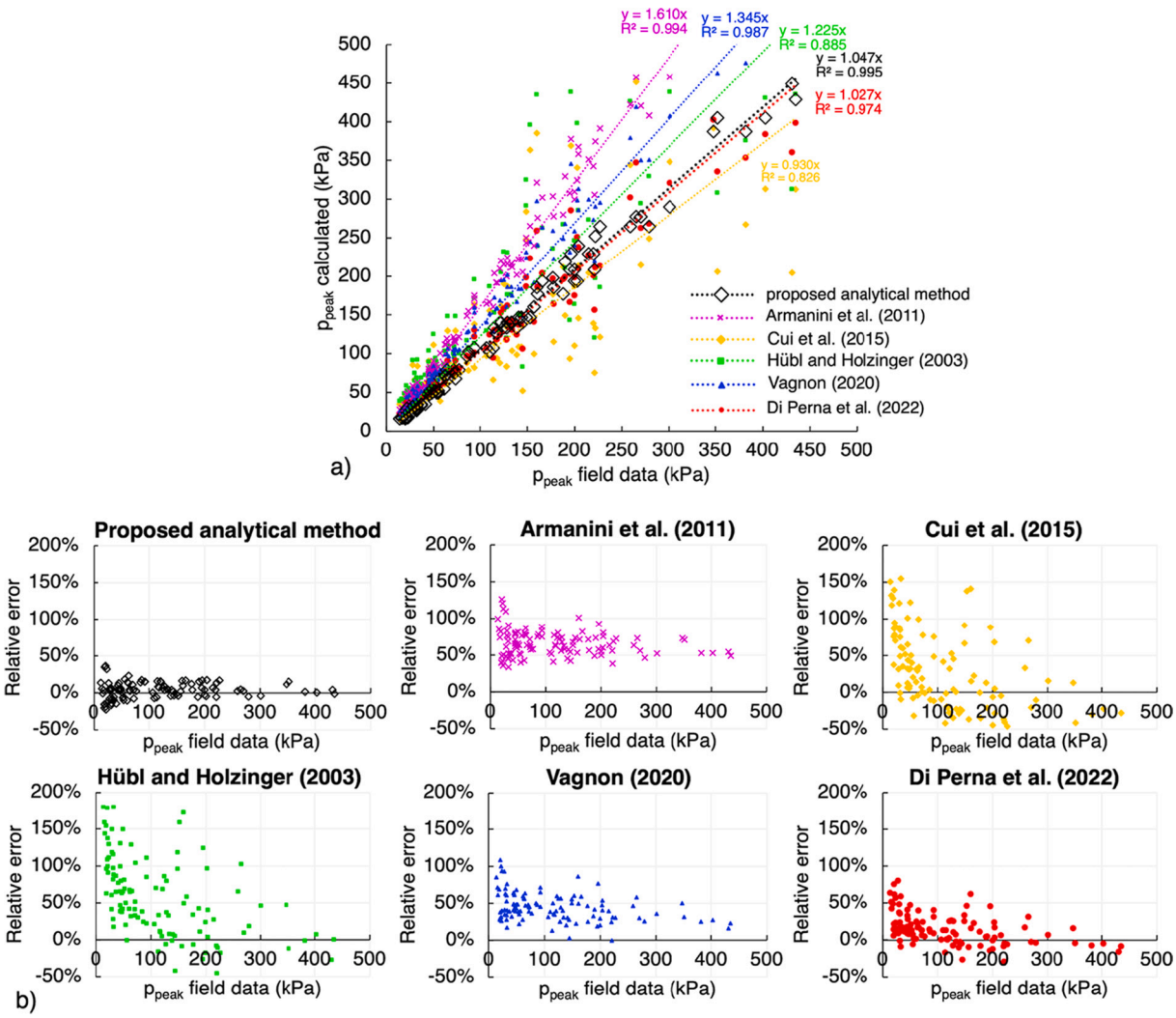

Fig. 15. The proposed analytical model compared to some empirical models available in the scientific literature (a) with the relative errors of each model (b).

proposed analytical model reports the highest correspondence among the real data and the computed values, also with a slight safe-side overestimation in the computed values. The empirical models of Armanini et al. (2011) and Vagnon (2020) are also acceptable with a contained dispersion of the calculated values and with an overestimated coefficient of 1.61 and 1.35, respectively (Fig. 15a). The formulations proposed by Hübl and Holzinger, 2003 and Cui et al. (2015) are, in contrast, characterized by a quite relevant variability of the achieved results. In particular, the method proposed by Cui et al. (2015) even leads to underestimate the peak values of impact pressure of about 7% (Fig. 15a).

Furthermore, the relative error between model prediction and field data is computed as $(p_{peak,\ calculated} - p_{peak,\ field\ data})/p_{peak,\ calculated}$ for each of the 139 impact pressure values (Fig. 15b). The comparison among all the methods highlight that the best estimate is obtained with the proposed analytical method, which is characterized by the lowest relative error, i.e., about ±10% for impact pressure values >50 kPa and up to ±30% for 0–50 kPa. Moreover, it emerges that some empirical models lead to a larger (and systematic) overestimation of the impact pressure. This is crucial for making a cost-effective design of the protection structure.

More in general, while the empirical models require as input data only the flow density, thickness and velocity, they can be used only for the design of fixed barriers, while not for DGRBs that are a promising landslide protection structure. The latter is instead well captured by both the proposed models, the MPM-based model and the energy-based analytical model.

5. Conclusions

This study has introduced and compared analytical and numerical MPM models to analyse the impact of flow-like landslides against artificial barriers, focusing not only on the evaluation of the peak impact forces but also on the kinematics evolution of both flow and barrier.

A conceptual model for the LSI problem was firstly introduced to better focalized the main variables that govern the dynamics of the impact process. This conceptual model was then implemented in a numerical Material Point Method (MPM) model and later used to propose a novel analytical impact model.

The calibration of the analytical model was conducted against the MPM outcomes to better monitor the most influential quantities for LSI problems, setting their values within the typical ranges for flow-type landslides. The achieved results reported that for the analytical model all the formulations depend on the calibrated parameter λ, which is found to be equal to 0.72 for fixed barrier and 0.41 for unfixed barriers.

The analytical model was validated through a real field dataset collected at Jiangjia Ravine (China), to check its predicting capability. The achieved results are encouraging, showing a high correspondence between the analytical model results and the measured field data.

A discussion on strengths and limitations of the two proposed models

was conducted and can summarized as follows:

1. MPM is an advanced numerical model and referring to LSI problems can handle a wide range of variables for both flow and barrier. Apart from this, MPM is a comprehensive method that allows to simulate the entire process of a landslide, from triggering to final deposition. This aspect is particularly important when studying the impact of a landslide against a protection structure since the main weakness of analytical and empirical models is the pre-setting of the flow depth and velocity. The latter parameters are particularly difficult to predict or measure during debris flow event, leading to a high uncertainty of the models. However, the high computational cost and its limited diffusion until now to the research field leaves its use to a small group of engineers.
2. An analytical model can be preferable in practice for designing fixed or unfixed barriers that must resist under the impulsive action of flow landslide. Its strong point is principally the simplicity in computing the main principal quantities in the context of LSI. In addition, it furnishes a not exaggerated overestimate of the peak impact pressures compared to those measured in the field.
3. Both the numerical and the analytical models here proposed are 2D approaches. Real landslides have a fully 3D evolution, that must be accurately treated in the triggering and propagation analyses. Indeed, also LSI is a 3D problem, but here the 3D effects are not considered in favour of less time-consuming computation.

In conclusion, the models proposed in this study show a good capability to predict the impact dynamics and kinematics of LSI. Further measured field data obtained for both fixed and unfixed artificial barrier will be helpful to improve the predictability of the two (numerical and analytical) proposed models. This can be achieved only by monitoring barriers systems against real flow-like landslides, with the final goal of helping to design artificial protection barriers with increasing level of safety and reliability.

CRediT authorship contribution statement

Sabatino Cuomo: Conceptualization, Methodology, Writing – original draft. **Angela Di Perna:** Formal analysis, Validation, Visualization, Writing – review & editing. **Mario Martinelli:** Conceptualization, Methodology, Software, Supervision, Data curation.

Declaration of Competing Interest

The authors declare that they have no known competing financial interests or personal relationships that could have appeared to influence the work reported in this paper.

Data availability

Data will be made available on request.

Acknowledgments

The research was developed within the framework of Industrial Partnership PhD Course (POR Campania FSE 2014/2020). All the MPM simulations were performed using a version of Anura3D code developed by Deltares.

Appendix 1. Material Point Method model equations

One-phase formulation

The conservation of mass is reported in Eq. (A1) and is automatically satisfied as the solid mass remains constant in each MP during deformation.

$$\frac{d\rho}{dt} + \rho \nabla \bullet \mathbf{v} = \mathbf{0} \tag{A1}$$

The conservation of momentum includes the conservation of both linear and angular momentum. The former is represented by the equation of motion, even known as Newton's second law (Eq. (A2)), while the conservation of angular momentum refers to the symmetry condition of the stress matrix ($\boldsymbol{\sigma} = \boldsymbol{\sigma}^T$).

$$\rho \frac{d\mathbf{v}}{dt} = \nabla \boldsymbol{\sigma}^T + \rho \boldsymbol{g} \tag{A2}$$

Finally, the constitutive equation needs to be expressed to include the stress-strain dependency (Eq. (A3)). The term **D** is the stiffness matrix; $\dot{\boldsymbol{\sigma}}'$ and $\dot{\varepsilon}$ are the stress and strain rate tensors of the solid phase, respectively. Ω is the spin tensor and $\dot{\varepsilon}_{vol}$ is the volumetric strain increment. To simulate large deformations (Eq. (A3) is derived) the Jaumann's stress rate of Kirchhoff stress can be considered; on the other hand, the Cauchy one which is limited to small strain rate (Martinelli and Galavi, 2022).

$$\dot{\boldsymbol{\sigma}}' = \mathbf{D}\dot{\varepsilon} + \Omega\boldsymbol{\sigma}' - \boldsymbol{\sigma}'\Omega - \dot{\varepsilon}_{vol}\boldsymbol{\sigma}' \tag{A3}$$

In undrained conditions, the stress state can be described in terms of effective stresses. The excess pore pressures can be computed by means of the so-called Effective Stress Analysis (Eq. (A4)), which assumes strain compatibility between the solid skeleton and the interstitial liquid (Vermeer, 1993).

$$\Delta p_L = \mathrm{K}_L \Delta \varepsilon_{vol} \tag{A4}$$

The time integration scheme considered in MPM is explicit, since most of the dynamic problems, including wave or shock propagation, cannot be treated properly by an implicit integration which tends to smooth the solution (Fern et al., 2019).

Let's consider the critical time step Δt_{cr} as the time increment during which a wave with speed c crosses the smallest element length d (Eq. (A5)).

$$\Delta t_{cr} = \frac{d}{c} = \frac{d}{\sqrt{E/\rho}} \tag{A5}$$

The critical time step defines the biggest time increment which can be used for a stable calculation, but often it can't be estimated in case of non-linear problems. For this reason, the critical time step is multiplied by an additional factor C_{NB} (namely Courant number) in order to reach stability. The Courant number has values between 0 and 1. Generally, the smaller the Courant number and the smaller the time step, improving the accuracy of the numerical results.

Two-phase formulation

A saturated porous medium is schematized as a solid phase which represents the solid skeleton, whereas the liquid phase fills the voids among the grains. Each MP represents a volume of the mixture V, given by the sum of the solid V_S and liquid V_L phases volumes. The behaviour of a saturated porous medium is here described using only one set of MPs, in which the information about both the solid and liquid constituents is stored.

The velocity field of solid and liquid phases are both used, but the material points move throughout the mesh with the kinematics of the solid skeleton. The equations to be solved concern the balance of dynamic momentum of solid and liquid phases, the mass balances, and the constitutive relationships of solid and liquid phases. The accelerations of the two phases are the primary unknowns: the solid acceleration $\mathbf{a}_S$, which is calculated from the dynamic momentum balance of the solid phase (Eq. (A6)), and the liquid acceleration $\mathbf{a}_L$, which is obtained by solving the dynamic momentum balance of the liquid phase (Eq. (A7)). The interaction force between solid and liquid phases is governed by Darcy's law (Eq. (A8)). Numerically, these equations are solved at grid nodes considering the Galerkin method (Luo et al., 2008) with standard nodal shape functions and their solutions are used to update the MPs velocities and momentum of each phase. The strain rate $\dot{\boldsymbol{\varepsilon}}$ of MPs is computed from the nodal velocities obtained from the nodal momentum.

$$n_S\rho_S\mathbf{a}_S = \nabla \bullet (\sigma - np_L\mathbf{I}) + (\rho_m - n\rho_L)\mathbf{b} + \mathbf{f}_d \tag{A6}$$

$$\rho_L\mathbf{a}_L = \nabla p_L - \mathbf{f}_d \tag{A7}$$

$$\mathbf{f}_d = \frac{n\mu_L}{k}(\mathbf{v}_L - \mathbf{v}_S) \tag{A8}$$

The resolution of solid and liquid constitutive laws (Eqs. (A9)–(A10)) allows calculating the increment of effective stress $d\boldsymbol{\sigma}'$ and excess pore pressure dp_L, respectively. The mass balance equation of the solid skeleton is then used to update the porosity of each MP (Eq. (A11)), while the total mass balance serves to compute the volumetric strain rate of the liquid phase (Eq. (A12)) since fluxes due to spatial variations of liquid mass are neglected ($\nabla n\rho_L = 0$).

$$\mathrm{d}\boldsymbol{\sigma}' = \mathbf{D} \bullet \mathrm{d}\boldsymbol{\varepsilon} \tag{A9}$$

$$\mathrm{d}p_L = \mathbf{K}_L \bullet \mathrm{d}\varepsilon_{vol} \tag{A10}$$

$$\frac{Dn}{Dt} = n_S\nabla \bullet \mathbf{v}_S = \mathbf{0} \tag{A11}$$

$$\frac{D\varepsilon_{vol}}{Dt} = \frac{n_S}{n}\nabla \bullet \mathbf{v}_S + \nabla \bullet \mathbf{v}_L \tag{A12}$$

In the two-phase single-point formulation the liquid mass, and consequently the mass of the mixture, is not constant in each material point but can vary depending on porosity changes. Fluxes due to spatial variations of liquid mass are neglected and Darcy's law is used to model solid-liquid interaction forces. For this reason, this formulation is generally used in problems with small gradients of porosity, and laminar and stationary flow in slow velocity regime. However, this formulation proves to be suitable for studying flow-structured-interaction (Cuomo et al., 2021a, 2021b). The water is assumed linearly compressible via the bulk modulus of the fluid $\mathbf{K}_L$ and shear stresses in the liquid phase are neglected.

The current MPM code uses 3-node elements which suffer kinematic locking, which consists in the build-up of fictitious stiffness due to the inability to reproduce the correct deformation field (Mast et al., 2012). A technique used to mitigate volumetric locking is the strain smoothening technique, which consists of smoothing the volumetric strains over neighbouring cells. The reader can refer to Al-Kafaji (2013) for a detailed description.

Regarding the critical time step, the influence of permeability and liquid bulk modulus must be considered as well (Mieremet et al., 2016). In particular, the time step required for numerical stability is smaller in soil with lower permeability (Eq. (A13)).

$$\Delta t_{cr} = min\left(\frac{d}{\sqrt{(E + \mathbf{K}_L/n)/\rho_m}}; \frac{2(\rho_m + (1/n - 2)\rho_L)k_{sat}}{\rho_L\boldsymbol{g}}\right) \tag{A13}$$

The sliding modelling of the flowing mass on the rigid material is handled by a frictional Mohr-Coulomb strength criterion. The contact formulation was used to ensure that no interpenetration occurs, and the tangential forces are compatible with the shear strength along the contact. The reaction force acting on the structure at node j was calculated as in Eq. (A14).

$$F_j(t) = m_{j,S}\Delta a_{S,contact} + m_{j,L}\Delta a_{L,contact} \tag{A14}$$

The terms $\Delta a_{S,\ contact}$ and $\Delta a_{L,\ contact}$ are the change in acceleration induced by the contact formulation, for both solid and liquid phase, and $m_{i,\ S}$ and $m_{i,\ L}$ are the corresponding nodal masses. The total reaction force is the integral of the nodal reaction forces along the barrier.

Appendix 2. Analytical model equations

Impact governing equations ($t_{imp} < t < T_2$)

For the action-reaction principle, the mutual impact forces of body 1 (i.e., the landslide) and body 2 (i.e., the barrier) are equal and opposite. In the following, the quantities referring to body 1 will be taken into consideration.

According to Newton's second law of dynamics, the reaction force between two colliding bodies can be written as in Eq. (A15), where s is time-dependent and represents the longitudinal interacting length of the considered body.

$$F(s) = m_1\frac{dv_1}{ds_1} \bullet \frac{ds_1}{dt} \tag{A15}$$

The velocity variation can be supposed to be linear along x and can be computed through Eq. (A16), which consists in the ratio between the velocity

variation during the impact period (t_{imp}, T_2) and the maximum interacting length of body 1.

$$\frac{dv_1}{ds_1} = \frac{v_{1,0} - v_{CM}}{s_{1,max}} \tag{A16}$$

For inelastic collision, the final velocity v_{CM} of the two bodies is the same and can be obtained from the conservation of linear momentum of the system if there is no friction between the sliding bodies and the surface (Eq. (A17)). If $m_2 \to \infty$, the final velocity of the body 1 goes to zero. This is a valuable assumption for the case of a fixed barrier.

$$v_{CM} = \frac{m_1 v_{1,0} + m_2 v_{2,0}}{m_1 + m_2} \tag{A17}$$

During the collision between the two bodies, the kinetic energy of the system is not conserved and the total variation of kinetic energy of the system can be obtained from Eq. (A18).

$$\Delta E_k = \frac{1}{2}\left(m_1 {v_{1,0}}^2 + m_2 {v_{2,0}}^2\right) - \frac{1}{2}(m_1 + m_2){v_{CM}}^2 \tag{A18}$$

Using Eqs. (A15)–(A16), Eq. (A14) can be written as in Eq. (A19).

$$F(s) = \left(\frac{m_1 m_2}{m_1 + m_2}\right) \bullet \left(\frac{v_{1,0} - v_{2,0}}{s_{1,max}}\right) \bullet \frac{ds_1}{dt} = K_1 \bullet \frac{ds_1}{dt} \tag{A19}$$

It is worth noting that the quantity $K_1 = \left(\frac{m_1 m_2}{m_1 + m_2}\right) \bullet \left(\frac{v_{1,0} - v_{2,0}}{s_{1,max}}\right)$ is a characteristic of body 1. Let introduce a new variable q_1 such that multiplied by the maximum interaction length of the body 1 ($s_{1,\,max}$) gives the work done by the impact force (Eq. (A20)).

The function $F(s)$ is not known a priori since $\frac{ds_1}{dt}$ is unknown. For this reason, the trend of F along s is assumed to be less than linear (Eq. (A21)), because this assumption considers the fact once the interaction has started, the additional volumes interacting with the barrier generate smaller and smaller increases in impact pressure with time.

From Eqs. (A18) and (A20), the variation of $\frac{ds_1}{dt}$ (Eq. (A22)) and the relationship between s_1 and t (Eq. (A23)) can be determined. The unknown quantities q_1 and T_2 can be obtained by solving the system in Eq. (A24), which reports the understandable conditions: (i) the integral of s_1 over the impact time is equal to the maximum interacting length ($s_{1,\,max}$) and (ii) the work done by the impact force is equal to the dissipated kinetic energy by the system (ΔE_k in Eq. (A18)). The formulations of T_2 and q_1 obtained by solving the system in Eq. (A24) are reported in Eqs. (A25)–(A26), respectively.

$$q_1 s_{1,max} = \int_0^{s_{1,max}} F(s) ds_1 \tag{A20}$$

$$F(s) = q_1 \sqrt{s_1} \tag{A21}$$

$$\frac{ds_1}{dt} = \frac{1}{2}\left(\frac{q_1}{K_1}\right)^2 t \tag{A22}$$

$$s_1(t) = \frac{1}{4}\left(\frac{q_1}{K_1}\right)^2 t^2 \tag{A23}$$

$$\begin{cases} \int_0^{T_2} \frac{ds_1}{dt} dt = s_{1,max} \\ \int_0^{s_{1,max}} F(s) ds_1 = \Delta E_k \end{cases} \tag{A24}$$

$$T_2 = \frac{8}{3}\frac{s_{1,max}}{(v_{1,0} - v_{2,0})} \tag{A25}$$

$$q_1 = \frac{3}{4}\frac{K_1 (v_{1,0} - v_{2,0})}{\sqrt{s_{1,max}}} \tag{A26}$$

Once known the quantities involved in the evaluation of the impact force over time and along s, the trend of the acceleration (Eq. (A27)) can be obtained from Eqs. (A15) and (A22). The velocity of body 1 is simply the integral of acceleration over time (Eq. (A28)) and so the trend of kinetic energy over time can be computed (Eq. (A29)).

$$a_1(t) = \frac{q_1^2}{2K_1 m_1} t \tag{A27}$$

$$v_1(t) = v_{1,0} - \frac{q_1^2}{4K_1 m_1} t^2 \tag{A28}$$

$$E_{k,1}(t) = \frac{1}{2} m_1 v_1^2(t) \tag{A29}$$

The same equations can be obtained for the body 2, considering the quantities related to the barrier. However, the frictional contact along the base of barrier causes its deceleration and therefore must be considered in Eq. (A27). The deceleration is equal to ratio between the frictional contact force and the mass of the barrier (Eq. (A30)) and remains constant during the interaction with the flow.

The formulation derived for the acceleration, velocity and kinetic energy of the barrier are reported in Eqs. (A31)–(A33), respectively. The barrier displacement Δx (Fig. 8) can be obtained by integrating the velocity trend over time (Eq. (A34)).

$$\left|a_{fr}\right| = \frac{F_{fr}}{m_2} = \frac{m_2 g tan(\delta_b)}{m_2} = g tan(\delta_b) \tag{A30}$$

$$a_2(t) = \frac{q_2^2}{2K_2 m_2} t - g tan(\delta_b) \tag{A31}$$

$$v_2(t) = v_{2,0} - g tan(\delta_b) t + \frac{q_2^2}{4K_2 m_2} t^2 \tag{A32}$$

$$E_{k,2}(t) = \frac{1}{2} m_2 v_2^2(t) \tag{A33}$$

$$\Delta x(t) = v_{2,0} - \frac{g}{2} tan(\delta_b) t^2 + \frac{q_2^2}{12K_2 m_2} t^3 \tag{A34}$$

The presented formulations consider that the impact force trend over time is a linear function that reaches the peak value at $t = T_2$. However, many studies (e.g. Song et al., 2017,) have demonstrated that the total impact force-time history can be simplified as a triangular force impulse, usually with a rise time (T_1) much shorter than the decay time ($T_2 - T_1$), as shown in Fig. 1. To consider this more realistic trend, the above-mentioned formulations can be rewritten, introducing the dimensionless ratio $\tau = \frac{T_1}{T_2}$ in such a way that the different triangular trends ($t_{imp} - F_{peak} - T_2$) all have the same area (i.e., the impulse of the impact force does not change with τ). To this aim, the general formulation $f(t)$ is converted into a new one $f(t')$ through a change of variables from t to t', as reported in Eq. (A35), see Fig. 9.

$$\begin{cases} f(t') = f\left(\frac{t}{\tau}\right) & 0 < t' < T_1 \\ f(t') = f\left(\frac{T_2 - t}{1 - \tau}\right) & T_1 < t' < T_2 \end{cases} \tag{A35}$$

Inertia governing equations ($T_2 < t < t_f$)

After impact, the interaction between the two bodies can be neglected since the motion is mostly governed by the friction at the base. In this stage, the change in velocity over time (Eq. (A36)) can be calculated referring to the uniformly decelerated motion equations, with the constant acceleration reported in Eq. (A30).

Since the barrier is assumed to slide over the distance Δx, the amount of energy that has been transferred to the barrier $E_{k,\,2}(T_2)$ is equal to the amount of energy dissipated by friction ($W_{fr} = F_{fr}\Delta x$).

The final displacement Δx_f of the barrier (Fig. 8d) is simply the sum of Eq. (A34) with $t = T_2$ and Eq. (A37), as reported in Eq. (A38).

$$v_{INERTIA}(t) = v_{CM} - \left|a_{fr}\right| \Delta t = v_{CM} - g\ tan(\delta_b)\ (t - T_2) \tag{A36}$$

$$\Delta x = \frac{{v_{CM}}^2}{2g\ tan(\delta_b)} \tag{A37}$$

$$\Delta x_f = \frac{{v_{CM}}^2}{2g\ tan(\delta_b)} + v_{2,0} T_2 - \frac{g}{2} tan(\delta_b) {T_2}^2 + \frac{q_2^2}{12K_2 m_2} {T_2}^3 \tag{A38}$$

References

Al-Kafaji, I., 2013. Formulation of a Dynamic Material Point Method (MPM) for Geomechanical Problems. Ph.D. thesis. University of Stuttgart.

Arattano, M., Franzi, L.J.N.H., 2003. On the evaluation of debris flows dynamics by means of mathematical models. Nat. Hazards Earth Syst. Sci. 3 (6), 539–544.

Armanini, A., Larcher, M., Odorizzi, M., 2011. Dynamic impact of a debris flow front against a vertical wall. In: In Proceedings of the 5th International Conference on Debris-Flow Hazards Mitigation: Mechanics, Prediction and Assessment, Padua, Italy, pp. 1041–1049.

Ashwood, W., Hungr, O., 2016. Estimating total resisting force in flexible barrier impacted by a granular avalanche using physical and numerical modeling. Can. Geotech. J. 53 (10), 1700–1717.

Bugnion, L., McArdell, B.W., Bartelt, P., Wendeler, C., 2012. Measurements of hillslope debris flow impact pressure on obstacles. Landslides 9 (2), 179–187.

Bui, H.H., Fukagawa, R., 2013. An improved SPH method for saturated soils and its application to investigate the mechanisms of embankment failure: Case of hydrostatic pore-water pressure. Int. J. Numer. Anal. Methods Geomech. 37 (1), 31–50.

Calvetti, F., Di Prisco, C.G., Vairaktaris, E., 2017. DEM assessment of impact forces of dry granular masses on rigid barriers. Acta Geotech. 12 (1), 129–144.

Canelli, L., Ferrero, A.M., Migliazza, M., Segalini, A., 2012. Debris flow risk mitigation by the means of rigid and flexible barriers–experimental tests and impact analysis. Nat. Hazards Earth Syst. Sci. 12 (5), 1693–1699.

Ceccato, F., Beuth, L., Vermeer, P.A., Simonini, P., 2016. Two-phase material point method applied to the study of cone penetration. Comput. Geotech. 80, 440–452.

Ceccato, F., Yerro, A., Martinelli, M., 2018. Modelling Soil-Water Interaction with the Material Point Method. Evaluation of Single-Point and Double-Point Formulations. NUMGE, 25–29 June. Porto, Portugal.

Cui, P., Zeng, C., Lei, Y., 2015. Experimental analysis on the impact force of viscous debris flow. Earth Surf. Process. Landf. 40 (12), 1644–1655.

Cuomo, S., Prime, N., Iannone, A., Dufour, F., Cascini, L., Darve, F., 2013. Large deformation FEMLIP drained analysis of a vertical cut. Acta Geotech. 8 (2), 125–136.

Cuomo, S., Perna, A.D., Martinelli, M., 2020a. MPM modelling of buildings impacted by landslides. In: Workshop on World Landslide Forum. Springer, Cham, pp. 245–266.

Cuomo, S., Moretti, S., Frigo, L., Aversa, S., 2020b. Deformation mechanisms of deformable geosynthetics-reinforced barriers (DGRB) impacted by debris avalanches. Bull. Eng. Geol. Environ. 79 (2), 659–672.

Cuomo, S., Di Perna, A., Martinelli, M., 2021a. MPM hydro-mechanical modelling of flows impacting rigid walls. Can. Geotech. J. 58 (11), 1730–1743.

Cuomo, S., Di Perna, A., Martinelli, M., 2021b. Modelling the spatio-temporal evolution of a rainfall-induced retrogressive landslide in an unsaturated slope. Eng. Geol. 294, 106371.

De Natale, J.S., Iverson, R.M., Major, J.J., LaHusen, R.G., Fiegel, G.L., Duffy, J.D., 1999. Experimental Testing of Flexible Barriers for Containment of Debris Flows. US Department of the Interior, US Geological Survey, Reston.
Di Perna, A., 2022. Multi-Phase Large Deformation Modelling of Flow-like Landslide Interaction with Protection Structures. Ph.D. Dissertation. University of Salerno, p. 241.
Di Perna, A., Cuomo, S., Martinelli, M., 2022. Empirical formulation for debris flow impact and energy release. Geoenviron. Disasters 9 (1), 1–17.
Faug, T., 2015. Depth-averaged analytic solutions for free-surface granular flows impacting rigid walls down inclines. Phys. Rev. E 92 (6), 062310.
Fei, Y., Guo, Q., Wu, R., Huang, L., Gao, M., 2021. Revisiting Integration in the Material Point Method: a Scheme for Easier Separation and less Dissipation. ACM Trans. Graph. 40 (4).
Fern, E., Rohe, A., Soga, K., Alonso, E., 2019. The Material Point Method for Geotechnical Engineering. A Practical Guide. CRC Press.
Galavi, V., Martinelli, M., Elkadi, A., Ghasemi, P., Thijssen, R., 2019. Numerical simulation of impact driven offshore monopiles using the material point method. In: Proceedings of the XVII ECSMGE-2019 https://doi. Org/10.32075/17ECSMGE-2019-0758.
Ghasemi, P., Calvello, M., Martinelli, M., Galavi, V., Cuomo, S., 2018. MPM simulation of CPT and model calibration by inverse analysis. In: Proc. of the 4th International Symposium on Cone Penetration Testing (CPT'18), 21–22 June, 2018, Delft, The Netherlands, vol. 37, pp. 1–7.
He, S., Liu, W., Li, X., 2016. Prediction of impact force of debris flows based on distribution and size of particles. Environ. Earth Sci. 75 (4), 298.
Hong, Y., Wang, J.P., Li, D.Q., Cao, Z.J., Ng, C.W.W., Cui, P., 2015. Statistical and probabilistic analyses of impact pressure and discharge of debris flow from 139 events during 1961 and 2000 at Jiangjia Ravine, China. Eng. Geol. 187, 122–134.
Hübl, J., Holzinger, G., 2003. Entwicklung von Grundlagen zur Dimensionierung kronenoffener Bauwerke für die Geschiebebewirtschaftung in Wildbächen: Kleinmassstäbliche Modellversuche zur Wirkung von Murbrechern. In: WLS Report 50 Band 3. Engineering, Institute of Mountain Risk (in German).
Hübl, J., Suda, J., Proske, D., Kaitna, R., Scheidl, C., 2009. Debris flow impact estimation. In: In Proceedings of the 11th International Symposium on Water Management and Hydraulic Engineering, Ohrid, Macedonia, vol. 1, pp. 1–5.
Idelsohn, S.R., Oñate, E., Pin, F.D., 2004. The particle finite element method: a powerful tool to solve incompressible flows with free-surfaces and breaking waves. Int. J. Numer. Methods Eng. 61 (7), 964–989.
Iverson, R.M., 1997. The physics of debris flows. Rev. Geophys. 35 (3), 245–296.
Jassim, I., Stolle, D., Vermeer, P., 2013. Two-phase dynamic analysis by material point method. Int. J. Numer. Anal. Methods Geomech. 37 (15), 2502–2522.
Jeong, S., Lee, K., 2019. Analysis of the impact force of debris flows on a check dam by using a coupled Eulerian-Lagrangian (CEL) method. Comput. Geotech. 116, 103214.
Kang, Z.C., Cui, P., Wei, F.Q., He, S.F., 2007. Data Collection of Observation of Debris Flows in Jiangjia Ravine, Dongchuan Debris Flow Observation and Research Station (1995–2000).
Leonardi, A., Wittel, F.K., Mendoza, M., Vetter, R., Herrmann, H.J., 2016. Particle–fluid–structure interaction for debris flow impact on flexible barriers. Comp. Aided Civil Infrastruct. Eng. 31 (5), 323–333.
Li, X., Zhao, J., Soga, K., 2021. A new physically based impact model for debris flow. Géotechnique 71 (8), 674–685.
Luo, H., Baum, J.D., Löhner, R., 2008. A discontinuous Galerkin method based on a Taylor basis for the compressible flows on arbitrary grids. J. Comput. Phys. 227 (20), 8875–8893.
Martinelli, M., Galavi, V., 2021. Investigation of the Material Point Method in the simulation of Cone Penetration Tests in dry sand. Comput. Geotech. 130, 103923.
Martinelli, M., Galavi, V., 2022. An explicit coupled MPM formulation to simulate penetration problems in soils using quadrilateral elements. Comput. Geotech. 145, 104697.
Mast, C.M., Mackenzie-Helnwein, P., Arduino, P., Miller, G.R., Shin, W., 2012. Mitigating kinematic locking in the material point method. J. Comput. Phys. 231 (16), 5351–5373.
Mieremet, M.M.J., Stolle, D.F., Ceccato, F., Vuik, C., 2016. Numerical stability for modelling of dynamic two-phase interaction. Int. J. Numer. Anal. Methods Geomech. 40 (9), 1284–1294.
Moriguchi, S., Borja, R.I., Yashima, A., Sawada, K., 2009. Estimating the impact force generated by granular flow on a rigid obstruction. Acta Geotech. 4 (1), 57–71.
Ng, C.W.W., Choi, C.E., Koo, R., Goodwin, G.R., Song, D., Kwan, J.S., 2018. Dry granular flow interaction with dual-barrier systems. Géotechnique 68 (5), 386–399.
Proske, D., Suda, J., Hübl, J., 2011. Debris flow impact estimation for breakers. Georisk 5 (2), 143–155.
Qiu, G., Henke, S., Grabe, J., 2011. Application of a Coupled Eulerian–Lagrangian approach on geomechanical problems involving large deformations. Comput. Geotech. 38 (1), 30–39.
Rabczuk, T., Belytschko, T., 2004. Cracking particles: a simplified meshfree method for arbitrary evolving cracks. Int. J. Numer. Methods Eng. 61 (13), 2316–2343.
Rabczuk, T., Belytschko, T., 2007. A three-dimensional large deformation meshfree method for arbitrary evolving cracks. Comput. Methods Appl. Mech. Eng. 196 (29–30), 2777–2799.
Scheidl, C., Chiari, M., Kaitna, R., Müllegger, M., Krawtschuk, A., Zimmermann, T., Proske, D., 2013. Analysing debris-flow impact models, based on a small scale modelling approach. Surv. Geophys. 34 (1), 121–140.
Scotton, P., Deganutti, A.M., 1997. Phreatic Line and Dynamic Impact in Laboratory Debris Flow Experiments.
Shen, W., Zhao, T., Zhao, J., Dai, F., Zhou, G.G., 2018. Quantifying the impact of dry debris flow against a rigid barrier by DEM analyses. Eng. Geol. 241, 86–96.
Soga, K., Alonso, E., Yerro, A., Kumar, K., Bandara, S., 2016. Trends in large-deformation analysis of landslide mass movements with particular emphasis on the material point method. Géotechnique 66 (3), 248–273.
Song, D., Ng, C.W.W., Choi, C.E., Zhou, G.G., Kwan, J.S., Koo, R.C.H., 2017. Influence of debris flow solid fraction on rigid barrier impact. Can. Geotech. J. 54 (10), 1421–1434.
Song, D., Zhou, G.G., Chen, X.Q., Li, J., Wang, A., Peng, P., Xue, K.X., 2021. General equations for landslide-debris impact and their application to debris-flow flexible barrier. Eng. Geol. 288, 106154.
Sulsky, D., Zhou, S.J., Schreyer, H.L., 1995. Application of a particle-in-cell method to solid mechanics. Comput. Phys. Commun. 87 (1–2), 236–252.
Thouret, J.C., Antoine, S., Magill, C., Ollier, C., 2020. Lahars and debris flows: Characteristics and impacts. Earth Sci. Rev. 201, 103003.
Vagnon, F., 2020. Design of active debris flow mitigation measures: a comprehensive analysis of existing impact models. Landslides 17 (2), 313–333.
Vagnon, F., Segalini, A., 2016. Debris flow impact estimation on a rigid barrier. Nat. Hazards Earth Syst. Sci. 16 (7), 1691–1697.
Vermeer, P.A., 1993. PLAXIS 2D Reference Manual Version 5. Balkema, Rotterdam / Brookfield.
Yong, A.C., Lam, C., Lam, N.T., Perera, J.S., Kwan, J.S., 2019. Analytical solution for estimating sliding displacement of rigid barriers subjected to boulder impact. J. Eng. Mech. 145 (3), 04019006.
Zambrano-Cruzatty, L., Yerro, A., 2020. Numerical simulation of a free fall penetrometer deployment using the material point method. Soils Found. 60 (3), 668–682.
Zhang, J., Xiong, G., 1997. Data Collection of Kinematic Observation of Debris Flows in Jiangjia Ravine, Dongchuan, Yunnan (1987–1994).
Zhou, G.G.D., Song, D., Choi, C.E., Pasuto, A., Sun, Q.C., Dai, D.F., 2018. Surge impact behavior of granular flows: effects of water content. Landslides 15 (4), 695–709.